UNIVERSITY OF OKLAHOMA
GRADUATE COLLEGE

UTILIZING FLOW PERFUSION BIOREACTOR SYSTEMS AS NOVEL PLATFORMS FOR CANCER RESEARCH

A THESIS
SUBMITTED TO THE GRADUATE FACULTY
in partial fulfillment of the requirements for the
Degree of
MASTER OF SCIENCE

By
PARKER REESE BRYANT
Norman, Oklahoma
2023

UTILIZING FLOW PERFUSION BIOREACTOR SYSTEMS AS NOVEL PLATFORMS FOR CANCER RESEARCH

A THESIS APPROVED FOR THE
STEPHENSON SCHOOL OF BIOMEDICAL ENGINEERING

BY THE COMMITTEE CONSISTING OF

Dr. Vassilios Sikavitsas, Chair

Dr. Roger H. Harrison

Dr. Edgar O'Rear

Acknowledgments

Firstly, I'd like to thank my family for not only allowing me to continue my education but also continuing to push me to achieve more. I'd like to thank my mother for always being there at any time, no matter how ridiculous the request, and always keeping me on track. I would also like to thank my father for teaching me all his technical skills and always fostering my curiosity by letting me hold the flashlight as a child. Furthermore, I'd like to thank my sister for constantly caring and checking in with me throughout my education career. Additionally, I owe so much to all my grandparents, who helped make attaining a college education feasible. I want to thank my Papa Clem for always answering the phone, giving excellent life advice, and helping cover the exorbitant expenses for school. Also, I would like to thank my Grandma Connie and Grandpa Arnold for ensuring I was fed and cared for throughout my life.

I want to thank the staff and faculty in the SBME and CBME departments for always motivating me and continually investing in me. I owe a special debt of gratitude to my advisor, Dr. Sikavitsas, who not only helped guide me in my education and research but also in life. In particular, thanks to Dr. Edgar O'Rear, Dr. Harrison, and Dr. Shambaugh for their constant guidance, and Madena McGinnis and Terri Colliver for always putting up with my constant shipments and questions.

Additionally, I would like to thank the other graduate students who helped answer my endless stream of questions while keeping me sane. These students include Alexis Woodward, Gabriela Faria, Daniel Karami, and Kylie Foster. I am extremely grateful for all your friendships and help. Additionally, I would like to extend a special thanks to LaRue Felder, who must have been exhausted from talking about oxygen sensors.

Table of Contents

List of Tables

List of Figures

Abstract

Cancer remains a leading cause of death worldwide, with no signs of slowing down. In 2023 alone, the projected number of deaths from cancer is 600,000, with projected incidences at almost 2 million. Mortality rates have improved recently, but a cancer diagnosis still burdens patients and their families. This burden weighs on patients not only financially but also emotionally. For example, the average out-of-pocket patient cost is more than $2,000 and can be even higher for more aggressive types of cancer. Additionally, 2 in 3 cancer patients experience significant psychological stress due to their diagnosis. As such, cancer research is an increasingly important field that will only become more needed as birthrates rise and the population continues to live longer.

The current *in vitro* cancer models generally rely on 2D monolayer cell growth conformation that lacks the sophistication required to represent physiological tissues accurately. As such, many therapeutic screening studies that employ these models fail to translate well to clinical trials. Furthermore, the xenografted nude mouse model, the most commonly used in vivo animal model, lacks many critical immune components to represent drug response and survival rates correctly. Also, as anticancer strategies are moving away from cytotoxic styles of drugs and toward inhibitory and immunotherapeutic drugs, the use cases for the nude mouse model have diminished greatly. Thus, the need for novel 3D physiologically accurate *in vitro* cancer research models is apparent. Bioreactors, specifically flow-perfusion bioreactors, are uniquely poised to fill this void as exceptionally useful tools for cell culture that can create 3D macro-scale cultures for tissue engineering applications. They offer unique cell culture monitoring facilities through

modular sensors, particularly in the liquid phase, which leaves a gap for creating an analytical sensor for gas phase volatile metabolite detection.

As such, the abovementioned deficiencies with current 2D *in vitro* models and the lack of proper gas phase metabolite analysis pose the guiding questions for this manuscript: 1) "How can we use novel mid-IR laser spectrometry to monitor cell cultures in bioreactors?" and 2) "In what ways does hypoxia affect the proliferation and oxygen uptake rates of cancer cells in 3D *in vitro* flow-perfusion bioreactor models?". These questions will be answered by modifying the previously established flow-perfusion bioreactor system to incorporate 3D collagen hydrogel scaffolds as a more physiologically representative *in vitro* solid tumor model. The verification of successful cell culture was determined using cell growth and viability. Furthermore, cell culture within the solid tumor model was monitored using a novel Mid-IR laser spectrometer to detect acetaldehyde, a gas-phase metabolite, as a potential biomarker for cancer diagnosis. Further exploring the novel 3D *in vitro* solid tumor model illuminated the need to add hypoxia, a critical component of solid tumor pathophysiology, to create a better biomimetic model. The hypoxic component was added by directing the flow of the bioreactor such that media flowed through each chamber without reoxygenation in a series way, thus lowering the oxygen saturation stepwise. The following chapters of this investigation will focus on answering each of these questions in succession.

1. Background and Significance

Tissue engineering is a growing field that merges biology with engineering and looks to propel medicine forward by introducing novel tissue regeneration technologies. While the ultimate goal of tissue engineering is to regenerate whole tissues, this goal is still a far cry from the state of the art of the field. Today, tissue engineering is taking steps toward creating new platforms for accelerated tissue growth, biologics production, and controlled delivery. Much of the field has focused on systems like microfluidics for micro-scale drug testing. While useful, microfluidics systems lack the complexity needed to accurately represent the body's natural state of tissues. Platforms like bioreactors aim to fill this gap by achieving the growth of macro-scale tissues in hopes of more closely mimicking the *in vivo* tissue state. Recently, bioreactor platforms have been considered potentially promising cancer research platforms.

1.1 Significance of Cancer and Cancer Research

Cancer has remained one of the leading causes of death worldwide, with trends still showing increasing incidence rates in 2023 [1, 2]. In 2023 alone, the estimated number of cancer deaths is more than 600,000, and the total number of incidences is almost 2 million [2]. Although mortality rates have improved, cancer remains a considerable burden for patients and their families. The incumbrance of a cancer diagnosis weighs heavily on the emotions of those affected and their finances. For instance, the average monthly out-of-pocket patient cost for cancer treatment in the United States is $2,568 and can be even higher for more aggressive cancer types [3]. For example, the average total Medicare expenditure per patient on prostate cancer radiation therapy ranges from $7,948 to $13,522, which can place undue psychological stress on those affected [4, 5]. As such, the prevalence of patient psychological stress due to the

financial burden of a cancer diagnosis is as high as 2 in 3 patients, depending on associated risk factors [4]. Additionally, the total associated costs of cancers worldwide from 2020 to 2025 are projected to be upwards of $37.9 trillion, which places a significant tax on the global healthcare system that will continue to rise as birthrates increase and the population ages [6]. Thus, the need to bolster cancer research becomes ever more apparent. While cancer research and drug development are generally quite costly, the median return for $1 spent on R&D is $14.5, which indicates that this research has a high rate of return. Yet, drug prices are marked up to attain these profit levels, restricting drug availability [7]. Due to the high number of the population afflicted by cancer, research on this disease will be a global mainstay. Solving this problem will require interdisciplinary collaboration and countless resources, demonstrating the continuous need for new therapies and diagnostic tools.

1.2 Relevance of *in vitro* Cell Culture Platforms

In vitro cell culture platforms attempt to provide a cost-effective and time-efficient screening of potential new technologies. Traditional *in vitro* models rely upon 2D culture flasks that force cells to grow in a single monolayer conformation. While these models can be enhanced with hydrogels, such as collagen and alginate, they tend to lack the sophistication of *in vivo* models [8, 9]. Yet, this simplicity is one of their main attractors. *In vitro* models provide easily interpretable results due to streamlined environments and controlled variables. Additionally, these platforms offer researchers cost and time savings by side-stepping the need for animal studies. Generally, beginning studies in an *in vivo* animal model without first testing simple metrics in an *in vitro* model is unrealistic due to the higher cost associated with failure. Furthermore, *in vitro* models comply with the Institutional Animal Care & Use Committee's (IACUC) first two major guidelines regarding animal use in research, replace and reduce [10].

Utilization of *in vitro* models can minimize harm to lab animals. Recently, new *in vitro* platforms, such as microfluidics and bioreactors, have pushed the boundaries and attempted to replicate the *in vivo* environment closely, further reducing the need for animal models [11-13]. *In vitro* platforms have become increasingly relevant in many fields, none more so than tissue engineering.

1.2.1 Relevance in Tissue Engineering

The driving concept behind tissue engineering is the pursuit of the knowledge required to regenerate human tissues without the need for allografting. As such, *in vitro* platforms are vital to this goal. The need for novel and biomimetic *in vitro* platforms is a multidisciplinary problem requiring pooled knowledge from biomaterials, biology, engineering, pharma, etc. As such, designing *in vitro* platforms in a biomimetic way is not a trivial undertaking. These platforms require multiple components to function fully and can often be limited by size and cell quantity [14].

In tissue-engineered *in vitro* models, scaffolds are utilized as replacements for the naturally occurring ECM. The materials used for these scaffolds can vary depending on the desired tissue type. For example, polymers, ceramics, and metals are often used for bone tissue engineering [15, 16]. In the case of engineered tendons and ligaments, fibers or hydrogels tend to be used [17]. Often these models will require the use of mechanical and physical stimulation, cell co-culture, as well as fluid perfusion by the use of bioreactors. Through the use of *in vitro* models, a greater understanding of how the body's natural tissues function, especially in the 3D environment, can be achieved. Factors like nutrient diffusivity, oxygen tension, and fluid shear forces can be controlled to determine their effects on cultured cells [18]. *In vitro* platforms play a pivotal role in tissue engineering and will continue to become more critical as the field matures.

1.2.2 Relevance in Cancer Research

While cancer research still relies heavily upon *in vivo* tumor models, more complex *in vitro* models are becoming a critical first step in therapeutic testing. Whereas both *in vivo* and *in vitro* tumor models serve as complementary testing platforms in cancer research, the latter can serve as an effective preliminary screening tool. *In vitro* testing platforms vary in cancer research, ranging from 2D monolayer cultures to 3D spheroid cultures with corresponding microenvironments [19, 20]. As a testing platform, *in vitro* cell culture offers unique benefits, such as the ability to simultaneously test multiple cancer cell lines, more representative anatomy of solid tumors, and the exclusion of animal-to-animal variations. Many use cases exist for these platforms, including but not limited to drug screening, metastasis modeling, and radiation therapy response screening [19]. A review of clinical studies that utilized *in vitro* selected chemotherapy, which uses patient-specific cells in an *in vitro* tumor culture for screening agents for chemotherapeutic response, showed that this testing method was as good and often better than empirical chemotherapeutic selection [21]. While successful, the clinical trials selected did suffer from a lack of culture repeatability and clear testing protocols, demonstrating the need to create better *in vitro* models. A recent study limited to breast cancer used complex 3D *in vitro* tumor spheroids with co-cultured epithelial, endothelial, and tumor cells that demonstrated similar tumor chemotherapeutic response compared to tumors grown *in vivo* [22]. As such, the value of *in vitro* testing has only continued to increase as these models grow closer to accurate *in vivo* replication.

1.3 2D versus 3D *in vitro* Cell Culture Platforms

The widespread availability of 2D cell culture platforms is undoubtedly due to their simplicity, cost-effective nature, and wealth of experience with different cell types. While 2D

culture platforms offer a quick and easy cell expansion method, these platforms lack several critical components of natural tissue anatomy. The lack of these components can cause discrepancies between 2D *in vitro* experimentation and *in vivo* clinical testing [23]. For instance, the lack of an extracellular matrix (ECM) in 2D cultures causes significant differences in cell morphology and gene expression [24]. To fill the gap between 2D and *in vivo* models, systems like 3D *in vitro* cell culture platforms are being developed. For example, patient-cells derived from primary tissues have been used in cultured spheroids to select treatments and screen for responsivity to immunotherapy in multiple cancer types, including colorectal, breast, and lung [25-27]. These platforms aim to recapitulate the natural cell environments by including components like the ECM and multiple cell types [28]. Novel 3D *in vitro* models can also be used to analyze the metastatic capabilities of cancer cells and potential anti-metastatic drugs [27]. 3D *in vitro* models seek to improve the shortcomings of simpler 2D culture systems by retaining these components in a more complex system.

1.3.1 Limitations of 2D in vitro Culture Platforms

Cultures performed in a 2D environment are exceptionally simplified compared to *in vivo* conditions but can still provide valuable testing, such as scratch/wound healing assay and viability [29]. Yet, the applicability of these types of cell cultures is waning. Because 2D cultures are an oversimplification of the natural tissues, the results gathered from these cultures often do not translate well into animal or clinical studies. Such oversimplifications become further apparent in cancer drug development, with only ~10% of potential anti-cancer drugs succeeding due to lack of efficacy or toxicity [30-33]. The poor translation of successful drug screening in 2D testing to *in vivo* application questions the model's validity in screening these drugs. For instance, in a study performed by Voskoglou-Nomikos et al., the validity *in vitro* prediction of

Phase II clinical performance was analyzed, and it was found that in the case of noncytotoxic cancer drugs, these models failed to provide reliable predictions of success in clinical trials [34]. Additionally, of those prospective cancer drugs that make it to clinical trials, many fail in the later stages of development, ~40% in phase III clinical trials, which is more costly than earlier phases [31]. Interestingly, in a survey to determine the dominant pre-clinical drug screening models, ~66% of respondents claimed to use 2D *in vitro* cell cultures [33]. Thus, despite the limitations of standard 2D cell culture models, they are still widely used. As such, the downsides of 2D testing have driven researchers to alternative testing models that translate well to *in vivo* and clinical trials, namely 3D *in vitro* models that can better represent natural tumors and tumor response.

1.3.2 2D vs 3D in vitro vs 3D in vivo

When comparing 2D with 3D *in vitro,* it is essential to consider the ultimate goal of tissue engineering and cancer research applications in human *in vivo* environments. 3D *in vitro* cultures exhibit features more closely resembling these environments; features like gene expression and morphologies are altered dramatically between 2D and 3D environments [24, 35]. As such, 3D *in vitro* environments can illuminate potential red flags before studies progress excessively. One of the main selling points for 3D cultures is understanding diffusional limits in natural settings. In 2D cultures, cells generally have access to oxygen and nutrients immediately and abundantly due to the imposed monolayer growth pattern. However, in 3D environments, especially avascular environments like solid tumors and cell spheroids, gradients of oxygen and nutrients exist, thus, limiting cell growth potential [36]. The diffusional limitations in 3D cultures can also help gauge potential drug delivery and tumor penetration issues *in vivo* [37]. Specifically, oxygen-related diffusional limitations are becoming increasingly crucial in studying solid tumors. These tumors

experience a hypoxic core as oxygen struggles to penetrate the exterior cell layers. This forces inner tumor cells to rely heavily upon metabolic and genetic changes [38]. In addition, hypoxic tumor environments correlate to worse prognosis and increased drug resistance [39].

Furthermore, 3D culture environments allow the incorporation of ECM-like components that can promote ECM-related gene expression, like E-cadherin [40]. Due to the presence of ECM components, relevant and necessary testing like cell migration, metastasis/invasion, and vascularization can be performed to better understand these processes in primary tumors [41]. Cancer cells cultured in 3D environments also tend to undergo the epithelial-to-mesenchymal transition more readily [42, 43], which has been shown to play a prominent role in disease progression, metastasis/invasion, and drug resistance [44]. In addition to ECM-like components, 3D *in vitro* systems have begun implementing co-cultures, or a culture that includes multiple different cell types, with some even including immune-related cells [45]. In one study, the model used had cancer-associated fibroblasts in a co-culture with oral squamous cell carcinoma (OSCC) and observed an upregulation in genes related to oxidative phosphorylation and an improved ability to form spheroids [46]. While relevant for cancer, 3D *in vitro* co-cultures are also valuable for studying the therapeutic effects of mesenchymal stem cells in different target locations [47, 48].

Several factors must be considered when comparing 3D in vitro cultures to common animal models. For instance, nude mice, one of the most commonly used animal models, lack an immune system. Nude mice with xenografted tumors have been used similarly to 3D *in vitro* models, focusing primarily on anti-cancer drug screening [49]. Although this model was valuable in most cases for cytotoxic drug discovery [49], new anticancer strategies are moving away from these styles of drugs and towards inhibitory and immunotherapeutic drugs instead [50]. This

transition has limited the efficacy of the nude mouse xenograft model and ushered in the need for new, more advanced replacement models. Developing novel 3D *in vitro* models has filled this void by creating accurate, regarding *in vivo* environments, platforms for cancer research. In the search for modern inhibitory and immunotherapeutic anti-cancer drugs, 3D *in vitro* systems allow for a more controlled analysis of the exact inhibitory mechanisms due to less variability [51, 52], as well as a better understanding of immunotherapies thanks to developments in co-culture techniques [53, 54]. Moreover, the low efficacy of the nude mouse xenograft model has ushered in the need for new advanced replacement models. Developing novel 3D *in vitro* models can fill this void by creating accurate, regarding *in vivo* environments, platforms for cancer research. In the search for modern inhibitory and immunotherapeutic anti-cancer drugs, 3D *in vitro* systems allow for a more controlled analysis of the exact inhibitory mechanisms due to less variability [51, 52], as well as a better understanding of immunotherapies thanks to developments in co-culture techniques [53, 54].

1.3.3 3D Macro-scale Culture

Focusing on the ultimate goal of tissue engineering, the regeneration or creation of natural tissues, illuminates the necessity of macro-scale cultures. For tissue-engineered products to be practical, these products must be sizeable enough to replace or cover wound sites. One of the earliest tissue engineering targets was engineered skin grafts due to the almost 2D layered conformation of the skin, making this tissue one of the easiest to grow [55]. Many commercial tissue-engineered skin options exist today, employing different scaffolding materials and co-culture strategies [56]. However, products like this require long cell culture times (2-3 weeks) and come at a high cost, with some currently available products requiring upwards of $13,000 to cover 1% of the body's surface area [56]. Moreover, the available options lack crucial skin

components like sebaceous glands and hair follicles [56]. Current tissue-engineered products are limited by culture time, high production costs, and lack of complexity, all of which highlight the necessity for better macro-scale culture techniques. However, one of the major limiting factors in developing engineered tissues, and therefore 3D macro-scale cell cultures, is the lack of tissue vascularization. The size of viable engineered tissues is severely limited because most cells must be within 50-100 microns of a blood vessel [57]. Inadequate blood vessel formation presents a barrier for most tissue creation, especially in highly metabolically demanding tissues, such as skeletal muscle tissue [58]. Blood vessel formation is important for engineered tissues and vessel replacement in cases of ischemic diseases, such as atherosclerotic cardiovascular disease [59]. While 3D macro-scale cell cultures are fundamental to solving tissue engineering problems, they can also play a role in understanding tumor angiogenesis and oxygen gradients. Understanding how blood vessels form and affect the oxygen tension in solid tumors is a critical step in solving many cancer drug delivery problems [60].

1.4 Value of Bioreactor Platforms

Bioreactors provide unique platforms for various cell culture conditions and types, which supports their adoption in laboratory and production scale environments. In addition to their adaptable cell culture conditions, bioreactors provide the modularity to swap components and sensors. The capability to swap in different sensing modalities makes bioreactors advantageous for production and monitoring tools, especially in biologics production [61]. Bioreactor sensors also provide researchers with essential data and can enable more accurate and even real-time culture monitoring [62].

1.4.1 Current Bioreactor Platforms

There are many different types of bioreactors, including but not limited to stirred tank, bubble column, airlift, hollow fiber, see-saw, and flow-perfusion bioreactors. Each modality has unique benefits and drawbacks, making them extremely useful in various applications. The stirred tank bioreactor is one of the most widely used bioreactors due to its simplicity and well-understood capabilities and limitations [63, 64]. This type of bioreactor can accommodate many different mammalian cell and bacteria types, with potentially therapeutic cells like mesenchymal stem cells (MSCs) and human CAR-T cells showing promising growth in stirred tank bioreactors [65-67]. Stirred tank bioreactors also offer better scale-up potential than traditional cell culture techniques, hence their use in industrial processes. Bioreactors of this nature can reach sizes of over 2000L, making producing low-yield products viable. While currently the most commonly used bioreactors in industry, other bioreactors like hollow-fiber and mechanically stimulating bioreactors provide unique ways to produce therapeutics and regenerate tissues. For example, hollow-fiber bioreactors have been proven to work equally well as stirred tanks in exosome production platforms, which, when paired with the potentially therapeutic nature of MSC exosomes, could be highly beneficial moving forward [68-70]. Similarly, mechanically stimulating bioreactors play a pivotal role in developing engineered tendons and ligaments [71, 72]. As *in vitro* models become more complex, bioreactors appear to be a natural progression in creating new *in vitro* research and production platforms.

Furthermore, bioreactors can enable easy monitoring of cell cultures by adding modular sensors to detect nutrient inputs and cellular metabolite outputs. Generally, culture monitoring is done in the liquid phase using sensors like dissolved oxygen, pH, and glucose [73, 74]. However, this leaves a distinct lack of monitoring for volatile metabolite compounds in the gas phase.

While liquid phase monitoring is important for cell culture, it restricts detected molecules to predominantly system inputs like glucose and dissolved O_2, requiring researchers to predict the health of cultures based on uptake rates rather than direct results of metabolism. Techniques like gas chromatography-mass spectrometry (GC-MS) and IR spectrometry have been investigated as potential analytical tools for detecting volatile metabolites but lack the sensitivity needed to detect trace metabolites and the capability of real-time measurements. Thus, a hole in the market exists for a capable and sensitive real-time analytical tool for detecting trace gas-phase metabolites for cell culture monitoring.

1.4.2 Flow Perfusion Bioreactors

Of the bioreactors previously listed, this thesis focuses mainly on flow-perfusion bioreactors. This is due to their ease of use and capacity to provide cells with fluid shear stress stimulus. This stimulus is required for the successful culture of many different cell types, particularly in osteogenic cell culture, as it promotes bone growth and improves MSC to osteoblast differentiation [75]. The fluid flow characteristics of flow-perfusion bioreactors also bypass most diffusional mass transport limitations traditionally found in 3D *in vitro* scaffold designs [76, 77]. Flow-perfusion bioreactors also provide unique testing platforms compared to 2D *in vitro* or microfluidics. Microfluidic platforms, like organ-on-a-chip, have been effective for cancer research in diagnostics and therapeutic screening [78, 79] but lack the scale and complexity to realize the micro and macro tumor environment fully. Flow-perfusion bioreactors can maintain the benefits of microfluidics but on a macro-scale, thus, more accurately depicting the tumor environment on all scale levels [80, 81]. A flow-perfusion setup can also provide the opportunity to link different scaffolds together, which allows for variable upstream conditions.

Linking scaffolds can enable researchers to investigate cell signaling within the same bioreactor through fluid flow. For example, cancer cells could be placed upstream of immune cells, and signaling between the two scaffolds could be monitored through bulk media sampling.

1.5 Research Objectives

There were two main guiding questions, and each is represented with an objective below, which this investigation aimed to answer: 1) “How can we use novel mid-IR laser spectrometry to monitor cell cultures in bioreactors?” and 2) “In what ways does hypoxia affect the proliferation and oxygen uptake rates of cancer cells in 3D *in vitro* flow-perfusion bioreactor models?”.

1.5.1 Objective 1

The initial objective of this investigation (Chapter 2) was to utilize newly developed mid-IR laser spectrometers as potential tools for monitoring gas phase metabolites from cell cultures in flow-perfusion bioreactors and as potential new cancer diagnostic and detection instruments. The flow perfusion bioreactor also needed to be modified to allow for the culture of non-RGD adherent cancer cell lines. The viability of this monitoring tool and bioreactor modification was determined by analyzing gas phase metabolite production and cell growth in the EMT6 cell line, a commonly used solid tumor murine breast cancer model, throughout multiple bioreactor runs.

1.5.2 Objective 2

The secondary objective of this investigation (Chapter 3) was to quantify the level of and effects of hypoxia in 3D hydrogel tumor-like environments in flow-perfusion bioreactors. Dissolved oxygen concentrations were measured using phase detection of fluorescent indicators to quantify the levels of hypoxia within the bioreactor. The effects of the created hypoxia were

determined using cell-counting and viability testing. A spheroid mathematical model was also applied using empirically measured data to estimate the size of each scaffold's anoxic core.

1.6 References

[1] T. Vos *et al.*, "Global burden of 369 diseases and injuries in 204 countries and territories, 1990–2019: a systematic analysis for the Global Burden of Disease Study 2019," (in English), *The Lancet,* vol. 396, no. 10258, pp. 1204-1222, 2020-10-17 2020, doi: 10.1016/S0140-6736(20)30925-9.

[2] R. L. Siegel, K. D. Miller, N. S. Wagle, and A. Jemal, "Cancer statistics, 2023," (in en), *CA: A Cancer Journal for Clinicians,* vol. 73, no. 1, pp. 17-48, 2023 2023, doi: 10.3322/caac.21763.

[3] N. Iragorri, C. de Oliveira, N. Fitzgerald, and B. Essue, "The Out-of-Pocket Cost Burden of Cancer Care—A Systematic Literature Review," (in en), *Current Oncology,* vol. 28, no. 2, pp. 1216-1248, 2021/4 2021, doi: 10.3390/curroncol28020117.

[4] G. L. Smith *et al.*, "Financial Burdens of Cancer Treatment: A Systematic Review of Risk Factors and Outcomes," (in en_US), *Journal of the National Comprehensive Cancer Network,* vol. 17, no. 10, pp. 1184-1192, 2019/10/01 2019, doi: 10.6004/jnccn.2019.7305.

[5] A. A. Laviana, A. N. Luckenbaugh, and M. J. Resnick, "Trends in the Cost of Cancer Care: Beyond Drugs," *Journal of Clinical Oncology,* vol. 38, no. 4, pp. 316-322, 2020-2-1 2020, doi: 10.1200/JCO.19.01963.

[6] S. Chen *et al.*, "Estimates and Projections of the Global Economic Cost of 29 Cancers in 204 Countries and Territories From 2020 to 2050," *JAMA Oncology,* vol. 9, no. 4, pp. 465-472, 2023-04-01 2023, doi: 10.1001/jamaoncol.2022.7826.

[7] K. Tay-Teo, A. Ilbawi, and S. R. Hill, "Comparison of Sales Income and Research and Development Costs for FDA-Approved Cancer Drugs Sold by Originator Drug Companies," *JAMA Network Open,* vol. 2, no. 1, p. e186875, 2019-01-04 2019, doi: 10.1001/jamanetworkopen.2018.6875.

[8] Y. Nakashima, K. Tsusu, K. Minami, and Y. Nakanishi, "Development of a cell culture surface conversion technique using alginate thin film for evaluating effect upon cellular differentiation," (in eng), *The Review of Scientific Instruments,* vol. 85, no. 6, p. 065004, 2014-06 2014, doi: 10.1063/1.4884076.

[9] D. O'Sullivan, L. O'Neill, and P. Bourke, "Direct Plasma Deposition of Collagen on 96-Well Polystyrene Plates for Cell Culture," (in eng), *ACS omega,* vol. 5, no. 39, pp. 25069-25076, 2020-10-06 2020, doi: 10.1021/acsomega.0c02073.

[10] H. J. Curzer, G. Perry, M. C. Wallace, and D. Perry, "The Three Rs of Animal Research: What they Mean for the Institutional Animal Care and Use Committee and Why," (in eng), *Science and Engineering Ethics,* vol. 22, no. 2, pp. 549-565, 2016-04 2016, doi: 10.1007/s11948-015-9659-8.

[11] M. P. Storm *et al.*, "Hollow Fiber Bioreactors for In Vivo-like Mammalian Tissue Culture," (in eng), *Journal of Visualized Experiments: JoVE,* no. 111, p. 53431, 2016-05-26 2016, doi: 10.3791/53431.

[12] Q. Wu *et al.*, "Organ-on-a-chip: recent breakthroughs and future prospects," (in eng), *Biomedical Engineering Online,* vol. 19, no. 1, p. 9, 2020-02-12 2020, doi: 10.1186/s12938-020-0752-0.

[13] C. Ma, Y. Peng, H. Li, and W. Chen, "Organ-on-a-Chip: A New Paradigm for Drug Development," (in eng), *Trends in Pharmacological Sciences,* vol. 42, no. 2, pp. 119-133, 2021-02 2021, doi: 10.1016/j.tips.2020.11.009.

[14] D. P. Pacheco, N. S. Vargas, S. Visentin, and P. Petrini, "From tissue engineering to engineering tissues: the role and application of in vitro models," (in en), *Biomaterials Science,* vol. 9, no. 1, pp. 70-83, 2021 2021, doi: 10.1039/D0BM01097A.

[15] M. Rizwan, M. Hamdi, and W. J. Basirun, "Bioglass® 45S5-based composites for bone tissue engineering and functional applications," (in en), *Journal of Biomedical Materials Research Part A,* vol. 105, no. 11, pp. 3197-3223, 2017 2017, doi: 10.1002/jbm.a.36156.

[16] Y. Yang *et al.*, "Metal organic frameworks as a compatible reinforcement in a biopolymer bone scaffold," (in en), *Materials Chemistry Frontiers,* vol. 4, no. 3, pp. 973-984, 2020 2020, doi: 10.1039/C9QM00772E.

[17] D. Olvera, R. Schipani, B. N. Sathy, and D. J. Kelly, "Electrospinning of highly porous yet mechanically functional microfibrillar scaffolds at the human scale for ligament and tendon tissue engineering," (in en), *Biomedical Materials,* vol. 14, no. 3, p. 035016, 2019-04 2019, doi: 10.1088/1748-605X/ab0de1.

[18] M. L. Felder, A. D. Simmons, R. L. Shambaugh, and V. I. Sikavitsas, "Effects of Flow Rate on Mesenchymal Stem Cell Oxygen Consumption Rates in 3D Bone-Tissue-Engineered Constructs Cultured in Perfusion Bioreactor Systems," (in en), *Fluids,* vol. 5, no. 1, p. 30, 2020/3 2020, doi: 10.3390/fluids5010030.

[19] M. Kapałczyńska *et al.*, "2D and 3D cell cultures – a comparison of different types of cancer cell cultures," *Archives of Medical Science : AMS,* vol. 14, no. 4, pp. 910-919, 2018-6 2018, doi: 10.5114/aoms.2016.63743.

[20] B. Pinto, A. C. Henriques, P. M. A. Silva, and H. Bousbaa, "Three-Dimensional Spheroids as In Vitro Preclinical Models for Cancer Research," (in en), *Pharmaceutics,* vol. 12, no. 12, p. 1186, 2020/12 2020, doi: 10.3390/pharmaceutics12121186.

[21] P. Cortazar and B. E. Johnson, "Review of the Efficacy of Individualized Chemotherapy Selected by In Vitro Drug Sensitivity Testing for Patients With Cancer," *Journal of Clinical Oncology,* vol. 17, no. 5, pp. 1625-1625, 1999-05 1999, doi: 10.1200/JCO.1999.17.5.1625.

[22] G. Benton, G. DeGray, H. K. Kleinman, J. George, and I. Arnaoutova, "In Vitro Microtumors Provide a Physiologically Predictive Tool for Breast Cancer Therapeutic Screening," (in en), *PLOS ONE,* vol. 10, no. 4, p. e0123312, Apr 9, 2015 2015, doi: 10.1371/journal.pone.0123312.

[23] K. Bhadriraju and C. S. Chen, "Engineering cellular microenvironments to improve cell-based drug testing," (in eng), *Drug Discovery Today,* vol. 7, no. 11, pp. 612-620, 2002-06-01 2002, doi: 10.1016/s1359-6446(02)02273-0.

[24] A. Birgersdotter, R. Sandberg, and I. Ernberg, "Gene expression perturbation in vitro - A growing case for three-dimensional (3D) culture systems," *Seminars in Cancer Biology,* vol. 15, no. 5, pp. 405-412, Oct 2005, doi: 10.1016/j.semcancer.2005.06.009.

[25] N. Boucherit, L. Gorvel, and D. Olive, "3D Tumor Models and Their Use for the Testing of Immunotherapies," (in eng), *Front Immunol,* vol. 11, p. 603640, 2020, doi: 10.3389/fimmu.2020.603640.

[26] L. Wallstabe *et al.*, "ROR1-CAR T cells are effective against lung and breast cancer in advanced microphysiologic 3D tumor models," (in eng), *JCI Insight,* vol. 4, no. 18, Sep 19 2019, doi: 10.1172/jci.insight.126345.

[27] M. Paolillo *et al.*, "Stem-Like Cancer Cells in a Dynamic 3D Culture System: A Model to Study Metastatic Cell Adhesion and Anti-Cancer Drugs," (in en), *Cells,* vol. 8, no. 11, p. 1434, 2019/11 2019, doi: 10.3390/cells8111434.

[28] E.-T. Verjans, J. Doijen, W. Luyten, B. Landuyt, and L. Schoofs, "Three-dimensional cell culture models for anticancer drug screening: Worth the effort?," (in en), *Journal of Cellular Physiology,* vol. 233, no. 4, pp. 2993-3003, 2018 2018, doi: 10.1002/jcp.26052.

[29] R. van Horssen and T. L. M. ten Hagen, "Crossing barriers: The new dimension of 2D cell migration assays," (in en), *Journal of Cellular Physiology,* vol. 226, no. 1, pp. 288-290, 2011 2011, doi: 10.1002/jcp.22330.

[30] A. L. Hopkins, "Network pharmacology: the next paradigm in drug discovery," (in en), *Nature Chemical Biology,* vol. 4, no. 11, pp. 682-690, 2008-11 2008, doi: 10.1038/nchembio.118.

[31] I. Kola, "The State of Innovation in Drug Development," (in en), *Clinical Pharmacology & Therapeutics,* vol. 83, no. 2, pp. 227-230, 2008 2008, doi: 10.1038/sj.clpt.6100479.

[32] W. N. Hait, "Anticancer drug development: the grand challenges," (in en), *Nature Reviews Drug Discovery,* vol. 9, no. 4, pp. 253-254, 2010-04 2010, doi: 10.1038/nrd3144.

[33] S. Martinez-Pacheco and L. O'Driscoll, "Pre-Clinical In Vitro Models Used in Cancer Research: Results of a Worldwide Survey," *Cancers,* vol. 13, no. 23, p. 6033, 2021-11-30 2021, doi: 10.3390/cancers13236033.

[34] T. Voskoglou-Nomikos, J. L. Pater, and L. Seymour, "Clinical predictive value of the in vitro cell line, human xenograft, and mouse allograft preclinical cancer models," *Clinical cancer research,* vol. 9, no. 11, pp. 4227-4239, 2003.

[35] S. Breslin and L. O'Driscoll, "The relevance of using 3D cell cultures, in addition to 2D monolayer cultures, when evaluating breast cancer drug sensitivity and resistance," (in en), *Oncotarget,* vol. 7, no. 29, pp. 45745-45756, 2016-06-10 2016, doi: 10.18632/oncotarget.9935.

[36] C. Schmitz, I. Pepelanova, C. Ude, and A. Lavrentieva, "Studies on oxygen availability and the creation of natural and artificial oxygen gradients in gelatin-methacryloyl hydrogel 3D cell culture," (in en), *Journal of Tissue Engineering and Regenerative Medicine,* vol. 16, no. 11, pp. 977-986, 2022 2022, doi: 10.1002/term.3344.

[37] A. I. Minchinton and I. F. Tannock, "Drug penetration in solid tumours," (in en), *Nat Rev Cancer,* vol. 6, no. 8, pp. 583-92, Aug 2006, doi: 10.1038/nrc1893.

[38] F. Paredes, H. C. Williams, and A. S. Martin, "Metabolic adaptation in hypoxia and cancer," *Cancer letters,* vol. 502, pp. 133-142, 2021-4-01 2021, doi: 10.1016/j.canlet.2020.12.020.

[39] X. Jing *et al.*, "Role of hypoxia in cancer therapy by regulating the tumor microenvironment," *Molecular Cancer,* vol. 18, no. 1, 2019, doi: 10.1186/s12943-019-1089-9.

[40] Y. Petrenko, E. Syková, and Š. Kubinová, "The therapeutic potential of three-dimensional multipotent mesenchymal stromal cell spheroids," *Stem Cell Research & Therapy,* vol. 8, no. 1, p. 94, 2017-04-26 2017, doi: 10.1186/s13287-017-0558-6.

[41] J. B. Kim, "Three-dimensional tissue culture models in cancer biology," (in en), *Seminars in Cancer Biology,* vol. 15, no. 5, pp. 365-377, 2005-10-01 2005, doi: 10.1016/j.semcancer.2005.05.002.

[42] H. J. Hwang, M.-S. Oh, D. W. Lee, and H.-J. Kuh, "Multiplex quantitative analysis of stroma-mediated cancer cell invasion, matrix remodeling, and drug response in a 3D co-culture model of pancreatic tumor spheroids and stellate cells," *Journal of Experimental & Clinical Cancer Research : CR,* vol. 38, p. 258, 2019-6-14 2019, doi: 10.1186/s13046-019-1225-9.

[43] N. Petruk *et al.*, "CD73 facilitates EMT progression and promotes lung metastases in triple-negative breast cancer," (in en), *Scientific Reports,* vol. 11, no. 1, p. 6035, 2021-03-16 2021, doi: 10.1038/s41598-021-85379-z.

[44] Y. Yang *et al.*, "Comprehensive analysis of EMT-related genes and lncRNAs in the prognosis, immunity, and drug treatment of colorectal cancer," *Journal of Translational Medicine,* vol. 19, p. 391, 2021-9-15 2021, doi: 10.1186/s12967-021-03065-0.

[45] J. Kuen, D. Darowski, T. Kluge, and M. Majety, "Pancreatic cancer cell/fibroblast co-culture induces M2 like macrophages that influence therapeutic response in a 3D model," *PLoS ONE,* vol. 12, no. 7, p. e0182039, 2017-7-27 2017, doi: 10.1371/journal.pone.0182039.

[46] H. Zhao, E. Jiang, and Z. Shang, "3D Co-culture of Cancer-Associated Fibroblast with Oral Cancer Organoids," (in en), *Journal of Dental Research,* vol. 100, no. 2, pp. 201-208, 2021-02-01 2021, doi: 10.1177/0022034520956614.

[47] K. Carter *et al.*, "Characterizing the impact of 2D and 3D culture conditions on the therapeutic effects of human mesenchymal stem cell secretome on corneal wound healing in vitro and ex vivo," (in en), *Acta Biomaterialia,* vol. 99, pp. 247-257, 2019-11-01 2019, doi: 10.1016/j.actbio.2019.09.022.

[48] A. Esmaeili, S. Hosseini, A. Kamali, M. Hosseinzadeh, F. Shekari, and M. Baghaban Eslaminejad, "Co-aggregation of MSC/chondrocyte in a dynamic 3D culture elevates the therapeutic effect of secreted extracellular vesicles on osteoarthritis in a rat model," *Scientific Reports,* vol. 12, no. 1, 2022, doi: 10.1038/s41598-022-22592-4.

[49] L. R. Kelland, ""Of mice and men": values and liabilities of the athymic nude mouse model in anticancer drug development," (in en), *European Journal of Cancer,* vol. 40, no. 6, pp. 827-836, 2004-04-01 2004, doi: 10.1016/j.ejca.2003.11.028.

[50] D. Liu, "CAR-T "the living drugs", immune checkpoint inhibitors, and precision medicine: a new era of cancer therapy," (in en), *Journal of Hematology & Oncology,* vol. 12, no. 1, p. 113, 2019-11-08 2019, doi: 10.1186/s13045-019-0819-1.

[51] X. Wan, W. Wang, and Z. Liang, "Epigallocatechin-3-gallate inhibits the growth of three-dimensional in vitro models of neuroblastoma cell SH-SY5Y," *Molecular and Cellular Biochemistry,* vol. 476, no. 8, pp. 3141-3148, 2021 2021, doi: 10.1007/s11010-021-04154-w.

[52] F. Moreira-Silva *et al.*, "G9a inhibition by CM-272: Developing a novel anti-tumoral strategy for castration-resistant prostate cancer using 2D and 3D in vitro models," (in en), *Biomedicine & Pharmacotherapy,* vol. 150, p. 113031, 2022-06-01 2022, doi: 10.1016/j.biopha.2022.113031.

[53] C. Vitale, M. Marzagalli, S. Scaglione, A. Dondero, C. Bottino, and R. Castriconi, "Tumor Microenvironment and Hydrogel-Based 3D Cancer Models for In Vitro Testing Immunotherapies," *Cancers,* vol. 14, no. 4, p. 1013, 2022-2-17 2022, doi: 10.3390/cancers14041013.

[54] B. Xue, J. Schüler, C. M. Harrod, K. Lashuk, Z. Bomya, and K. C. Hribar, "A Novel Hydrogel-Based 3D In Vitro Tumor Panel of 30 PDX Models Incorporates Tumor,

Stromal and Immune Cell Compartments of the TME for the Screening of Oncology and Immuno-Therapies," (in eng), *Cells,* vol. 12, no. 8, p. 1145, 2023-04-13 2023, doi: 10.3390/cells12081145.

[55] F. Berthiaume, T. J. Maguire, and M. L. Yarmush, "Tissue Engineering and Regenerative Medicine: History, Progress, and Challenges," *Annual Review of Chemical and Biomolecular Engineering,* vol. 2, no. 1, pp. 403-430, 2011 2011, doi: 10.1146/annurev-chembioeng-061010-114257.

[56] K. Vig *et al.*, "Advances in Skin Regeneration Using Tissue Engineering," *International Journal of Molecular Sciences,* vol. 18, no. 4, p. 789, 2017-4-07 2017, doi: 10.3390/ijms18040789.

[57] B. Alberts, A. Johnson, J. Lewis, M. Raff, K. Roberts, and P. Walter, "Blood Vessels and Endothelial Cells," in *Molecular Biology of the Cell. 4th edition*: Garland Science, 2002.

[58] J. Gilbert-Honick and W. Grayson, "Vascularized and Innervated Skeletal Muscle Tissue Engineering," *Advanced healthcare materials,* vol. 9, no. 1, p. e1900626, 2020-1 2020, doi: 10.1002/adhm.201900626.

[59] H.-H. G. Song, R. T. Rumma, C. K. Ozaki, E. R. Edelman, and C. S. Chen, "Vascular tissue engineering: progress, challenges, and clinical promise," *Cell stem cell,* vol. 22, no. 3, pp. 340-354, 2018-3-01 2018, doi: 10.1016/j.stem.2018.02.009.

[60] S. M. Bhat *et al.*, "3D tumor angiogenesis models: recent advances and challenges," *Journal of Cancer Research and Clinical Oncology,* vol. 147, no. 12, pp. 3477-3494, 2021 2021, doi: 10.1007/s00432-021-03814-0.

[61] A. Glindkamp, D. Riechers, C. Rehbock, B. Hitzmann, T. Scheper, and K. F. Reardon, "Sensors in Disposable Bioreactors Status and Trends," in *Disposable Bioreactors*, R. Eibl and D. Eibl Eds., (Advances in Biochemical Engineering / Biotechnology. Berlin, Heidelberg: Springer, 2010, pp. 145-169.

[62] T. K. Karakach, A. Dachon, J. Choi, C. Miguez, L. Masson, and B. Tartakovsky, "Fluorescence-based real time monitoring and diagnostics of recombinant Pichia pastoris cultivations in a bioreactor," (in eng), *Biotechnology Progress,* vol. 35, no. 2, p. e2761, 2019-03 2019, doi: 10.1002/btpr.2761.

[63] F. Garcia-Ochoa and E. Gomez, "Bioreactor scale-up and oxygen transfer rate in microbial processes: An overview," (in en), *Biotechnology Advances,* vol. 27, no. 2, pp. 153-176, 2009-03-01 2009, doi: 10.1016/j.biotechadv.2008.10.006.

[64] E. Sajeev, S. Shekher, C. C. Ogbaga, K. S. Desongu, B. Gunes, and J. A. Okolie, "Application of Nanoparticles in Bioreactors to Enhance Mass Transfer during Syngas Fermentation," (in en), *Encyclopedia,* vol. 3, no. 2, pp. 387-395, 2023/6 2023, doi: 10.3390/encyclopedia3020025.

[65] A. Mizukami *et al.*, "Stirred tank bioreactor culture combined with serum-/xenogeneic-free culture medium enables an efficient expansion of umbilical cord-derived mesenchymal stem/stromal cells," (in eng), *Biotechnology Journal,* vol. 11, no. 8, pp. 1048-1059, 2016-08 2016, doi: 10.1002/biot.201500532.

[66] E. Costariol *et al.*, "Demonstrating the Manufacture of Human CAR-T Cells in an Automated Stirred-Tank Bioreactor," (in eng), *Biotechnology Journal,* vol. 15, no. 9, p. e2000177, 2020-09 2020, doi: 10.1002/biot.202000177.

[67] F. Ivušić, T. Rezić, and B. Šantek, "Heterotrophic Cultivation of Euglena gracilis in Stirred Tank Bioreactor: A Promising Bioprocess for Sustainable Paramylon Production," (in eng), *Molecules (Basel, Switzerland),* vol. 27, no. 18, p. 5866, 2022-09-09 2022, doi: 10.3390/molecules27185866.

[68] D. C. Watson *et al.*, "Efficient production and enhanced tumor delivery of engineered extracellular vesicles," *Biomaterials,* vol. 105, pp. 195-205, Oct 2016, doi: 10.1016/j.biomaterials.2016.07.003.

[69] Y. S. Chen, E. Y. Lin, T. W. Chiou, and H. J. Harn, "Exosomes in clinical trial and their production in compliance with good manufacturing practice," *Tzu Chi Medical Journal,* vol. 32, no. 2, pp. 113-120, Apr-Jun 2020, doi: 10.4103/tcmj.tcmj_182_19.

[70] W. Olejarz, G. Kubiak-Tomaszewska, A. Chrzanowska, and T. Lorenc, "Exosomes in Angiogenesis and Anti-angiogenic Therapy in Cancers," *International Journal of Molecular Sciences,* vol. 21, no. 16, Aug 2020, Art no. 5840, doi: 10.3390/ijms21165840.

[71] T. Wang *et al.*, "Bioreactor Design for Tendon/Ligament Engineering," *Tissue Engineering. Part B, Reviews,* vol. 19, no. 2, pp. 133-146, 2013-4 2013, doi: 10.1089/ten.teb.2012.0295.

[72] B. Engebretson, Z. R. Mussett, and V. I. Sikavitsas, "The effects of varying frequency and duration of mechanical stimulation on a tissue-engineered tendon construct," *Connective Tissue Research,* vol. 59, no. 2, pp. 167-177, 2018-03-04 2018, doi: 10.1080/03008207.2017.1324431.

[73] A. Simmons, C. Iii, A. Degoix, and V. Sikavitsas, "Sensing Metabolites for the Monitoring of Tissue Engineered Construct Cellularity in Perfusion Bioreactors," *Biosensors and Bioelectronics,* vol. 90, 09/30 2016, doi: 10.1016/j.bios.2016.09.094.

[74] A. D. Simmons and V. I. Sikavitsas, "Monitoring Bone Tissue Engineered (BTE) Constructs Based on the Shifting Metabolism of Differentiating Stem Cells," (in eng), *Ann Biomed Eng,* vol. 46, no. 1, pp. 37-47, Jan 2018, doi: 10.1007/s10439-017-1937-y.

[75] V. I. Sikavitsas *et al.*, "Fluid flow increases mineralized matrix deposition in three-dimensional perfusion culture of marrow stromal osteoblasts in a dose-dependent manner," in *Proceedings of the Second Joint 24th Annual Conference and the Annual Fall Meeting of the Biomedical Engineering Society] [Engineering in Medicine and Biology*, 2002-10 2002, vol. 1, pp. 884-885 vol.1, doi: 10.1109/IEMBS.2002.1137126.

[76] G. N. Bancroft, V. I. Sikavitsas, and A. G. Mikos, "Technical Note: Design of a Flow Perfusion Bioreactor System for Bone Tissue-Engineering Applications," *Tissue Engineering,* vol. 9, no. 3, pp. 549-554, 2003-06 2003, doi: 10.1089/107632703322066723.

[77] A. M. Gharravi, M. Orazizadeh, and M. Hashemitabar, "Fluid-induced low shear stress improves cartilage like tissue fabrication by encapsulating chondrocytes," (in en), *Cell and Tissue Banking,* vol. 17, no. 1, pp. 117-122, 2016-03-01 2016, doi: 10.1007/s10561-015-9529-2.

[78] S. Regmi, C. Poudel, R. Adhikari, and K. Q. Luo, "Applications of Microfluidics and Organ-on-a-Chip in Cancer Research," (in en), *Biosensors,* vol. 12, no. 7, p. 459, 2022/7 2022, doi: 10.3390/bios12070459.

[79] J. Sierra-Agudelo, R. Rodriguez-Trujillo, and J. Samitier, "Microfluidics for the Isolation and Detection of Circulating Tumor Cells," Springer International Publishing, 2022, pp. 389-412.

[80] D. Karami, N. Richbourg, and V. Sikavitsas, "Dynamic in vitro models for tumor tissue engineering," (in eng), *Cancer Letters,* vol. 449, pp. 178-185, 2019-05-01 2019, doi: 10.1016/j.canlet.2019.01.043.

[81] A. Pasini *et al.*, "Perfusion Flow Enhances Viability and Migratory Phenotype in 3D-Cultured Breast Cancer Cells," *Annals of Biomedical Engineering,* vol. 49, no. 9, pp. 2103-2113, 2021 2021, doi: 10.1007/s10439-021-02727-w.

2. Novel Gas Phase Metabolite Analysis for Perfusion Bioreactors with Mid IR-Laser Spectrometry

Abstract

Cancer cells demonstrate an abnormal metabolism, where cells prioritize glucose uptake, and glycolysis is preferred even in sufficient oxygen levels, known as the Warburg effect. This results in higher production levels of pyruvate and lactic acid, and since pyruvate decomposes to acetaldehyde and carbon dioxide, the concentration of acetaldehyde is expected to be higher in cancer cells expressing the Warburg phenotype. Because acetaldehyde has a relatively low normal boiling point, 20.2°C, it has a relatively high vapor pressure at 37°C, the typical physiological temperature. As such, acetaldehyde appears to be a potentially promising gas-phase metabolite biomarker of cancer. This study utilized a novel Mid-IR laser spectrometer to analyze the gas phase concentrations of acetaldehyde in the headspace of media from EMT6 murine breast cancer cells cultured in 3D hydrogel scaffolds in a flow-perfusion bioreactor system. Acetaldehyde concentrations were successfully measured in the parts-per-billion (ppb) range, with results showing sufficient production levels. Additionally, the impacts of hypoxia were investigated as a potential effector on the metabolic processing of glucose and, thus, the creation of acetaldehyde.

2.1 Introduction

2.1.1 Cancer Metabolism and the Warburg Effect

Most cancer cells are known to have altered metabolisms, such that glucose is broken down through glycolysis even in the presence of abundant oxygen. This has long been known and was first observed by Otto Warburg in 1924 [1] and has been dubbed "The Warburg Effect." To explain this phenomenon, Warburg hypothesized that the mitochondria were damaged and not functioning in cancer cells [2]. While mitochondrial damage can play a role in the Warburg effect, it is now heavily attributed to the lack of tumor suppressor gene expression and overexpression of oncogenes. Additionally, the activation of the transcription factor hypoxia-inducible factor (HIF)-1α in normoxic and hypoxic conditions plays a critical role in the hallmark aerobic glycolysis of the Warburg effect. While originally thought to be a universal causal factor of carcinogenesis, the Warburg effect is only apparent in 70%-80% of cancers, indicating it is a symptom of certain cancers rather than a cause [3]. A Warburg style of metabolism can also be found in other rapidly proliferating mammalian cells like stem cells, endothelial cells, and even early-stage mammalian embryos [3], thus, suggesting the shift is a transition to a biosynthesis-focused metabolism to support cellular growth. The Warburg effect enables rapid proliferation and the synthesis of cellular components through multiple transcription factors and pathways. However, of these, the activation of the HIF-1α transcription factor and Phosphatidylinositol-3-kinase (P13K)/Akt/ mammalian target of rapamycin (mTOR) pathways, as well as deactivation of the threonine kinase liver kinase B1 (LKB1)/ AMP-activated protein kinase (AMPK) pathways and cMYC transcription factors are the key dysregulations [2, 4, 5].

The glycolytic pathway (Figure 2.1) involves 9-10 steps that catabolize glucose into pyruvate generating 2 ATP. While much less efficient concerning glucose consumption, compared to oxidative phosphorylation (OXPHOS), intermediate products in this pathway are critical in synthesizing various cellular components [3].

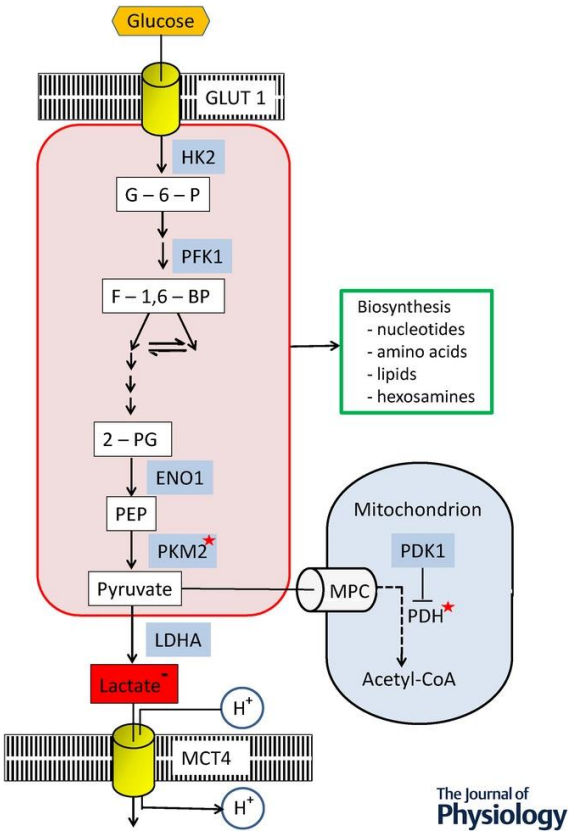

Figure 2.1: Key Steps in the Glycolytic Pathway

Diagram of the glycolytic pathway in cells expressing the Warburg phenotype. Glucose uptake increases as GLUT-1 receptors are overexpressed and converted to 2 pyruvate and 2 ATP molecules, the final product of aerobic glycolysis. Less functional gatekeeper enzymes (red star) can result in accumulated glucose-derived biosynthesis products. Figure used with permission from the following publication [3].

Interestingly, cancer cells can act as glucose traps through the decreased activity of the pyruvate kinase (PK) enzyme responsible for catalyzing the conversion of phosphoenolpyruvate (PEP) to

pyruvate [2]. The activation of HIF-1α and P13K pathways can prompt the transcription of the M2 dimeric isoform of pyruvate kinase (PKM2), which is almost entirely inactive, accumulating glucose-derived biosynthesis products [2, 3]. HIF-1α activation can also facilitate the production of characteristically high levels of lactic acid observed from the Warburg effect. Through both cMYC and HIF-1α activation, the expression of pyruvate dehydrogenase kinase 1 (PDK-1), which prevents pyruvate from entering the mitochondria, and lactate dehydrogenase A (LDH-A), which catalyzes cytosolic pyruvate reduction into lactate, is increased [2, 6]. In addition to biosynthesis-related molecules, increased glucose uptake can cause cellular pyruvate accumulation [7]. Recently, it has been discovered that increased lactate concentrations around tumors can act as an energy-rich substrate for oxidative cells, preserving glucose for less oxygenated glycolytic cells [8]. As an alternative to glucose uptake and glycolysis, the outermost cancer cells can take up lactate, which can then be oxidized into pyruvate and NADH to fuel the TCA cycle. Monocarboxylate transporters (MCT), specifically MCT1 and MCT4, are critical to balancing lactate uptake and export [8]. The expression of MCTs varies from cancer to cancer but is generally overexpressed [8]. The oxidation of lactate into pyruvate again indicates a potential increased pyruvate concentration in cancer cells. Thus, the Warburg effect, the characteristic abnormal metabolism characteristic of most cancer cells, can provide unique diagnostic and therapeutic targets as potential cancer fingerprinting techniques.

2.1.2 Traditional Bioreactor Monitoring Systems

Generally, sensors used in industry bioreactors are older technologies and lack the sophistication needed to provide whole-system monitoring. Sensors like the Clark-type dO sensors and glass pH electrodes are limited in their usefulness due to stationary positioning, which limits their ability to sample entire systems, as well as their fragility and multiple-use

nature, which can complicate the cleaning and cleaning validation [9]. To combat this, the biopharmaceutical industry has begun to switch to single-use bioreactors, generally multi-layered sterilized plastic bags that offer efficient cleaning and cleaning validation; however, fragile multiple-use sensors limit this efficiency [10]. Additionally, regulating agencies have begun to push biopharmaceutical companies to place more emphasis on process monitoring to ensure drug quality, specifically critical process parameters [11]. These parameters can be correlated to drug quality and are restricted to ensure satisfactory results. Thus, development in sensing technologies is still required to achieve the level of control needed to optimize production processes fully.

Currently used sensors traditionally focus on liquid phase monitoring of key cell nutrients and bulk system parameters. Arguably the most commonly measured bioreactor parameter, pH, is vital for maintaining cell viability and growth rates [9, 12]. While there are multiple ways to achieve pH measurements, steam-sterilizable glass electrode sensors are the most common. This is due to how well-understood these sensors are. However, their fragility and bulky size have prompted research into alternative options [12]. Optical pH sensors utilize pH-variable dyes of fluorescence and absorbance modalities to determine the hydrogen ion concentration in solution [12, 13]. Dissolved oxygen is another critical nutrient commonly monitored because it directly limits cell growth potential. Like pH, this has traditionally been performed using electrochemical Clark-type sensors but has shifted towards optical sensors [14]. Optical dissolved oxygen sensors work such that a fluorescent dye is embedded in a silicon rubber patch. This patch is then exposed to dissolved oxygen which quenches the measured fluorescence intensity in a quantifiable manner by the Stern-Volmer equation [14, 15].

While optical sensors have shown promise, they have not matured enough to mitigate their drawbacks. For instance, optical sensors tend to drift over time due to photobleaching and instability. Additionally, these sensors are affected by environmental conditions like sudden light source changes or different external light levels [14]. As an alternative method, some commercially available optical dissolved oxygen sensors measure changes in phase angle between the excitation of a modulated light source and the emission of a fluorescent dye. This can mitigate the effects of light source stability and photobleaching, providing sensors with longer stable lifetimes and more accurate readings [14]. However, this is still not a perfect solution, as these sensors still have much shorter lifespans, less than bioreactor run lengths, compared to electrochemical Clark-type sensors. Yet, optical metabolite sensing solutions may be better suited to single-use bioreactor systems, thus, lowering the bar for stable lifetime length. As such, these sensors have become a significant focus for the bioreactor industry and will continue to play a prominent role in biopharmaceuticals' quality assurance.

2.1.3 Need for Gas Phase Monitoring

While the abovementioned sensors work great for monitoring bioreactor systems' liquid phase, this is often limited to input parameters. Metabolites and output products are not as commonly measured, forcing researchers and companies to predict cell culture status rather than looking at the whole picture. One of the most overlooked cell culture monitoring methods is the analysis of the gas phase nutrients and metabolites. The existing gas phase monitoring methodologies also focus on nutrients and metabolites that can be easily measured in the liquid phase, like oxygen [16, 17]. Many volatile mammalian cell metabolites, like ethanol and acetaldehyde, can be measured in the gas phase using varying gas analysis methods [18].

Acetaldehyde, an exciting volatile metabolite target, is readily produced exothermically from pyruvate. The energy of formation of this reaction was calculated in Table 2.1 below.

Table 2.1: Energy of Formation for the Decarboxylation of Pyruvate to Acetaldehyde

Energies of formation, at 37°C, for $C_3H_4O_3(aq) \longrightarrow CH_3CHO(aq) + CO_2(g)$ *at different ionic strengths, as in biological systems during active ATP-driven hydrolysis. These energies were calculated using Gibbs free energy, G = H –TS, and enthalpy and entropy of formation data from [19].*

	Ionic Strength (mol/l)	0.00	0.10	0.25
Energy of Formation, ΔG_f (kJ/mol) at 37°C	- $C_3H_4O_3$ (pyruvate)	-342.6	-341.3	-340.9
	+ CH_3CHO (acetaldehyde)	30.2	32.8	33.6
	+ CO_2	-394.4	-394.4	-394.4
ΔG for pyruvate decarboxylation		**-21.6**	**-20.3**	**-19.9**

This metabolite has a relatively low boiling point of 20.2°C and, as such, should have a high vapor pressure (1315.6 mmHg) at 37°C entering the gas phase reasonably easily [20]. As aforementioned, in many cancers, there can be an excess of pyruvate, thus indicating a potential increase in acetaldehyde production. These properties imply that this metabolite may be a potentially favorable biomarker for cancer diagnosis. Additionally, the cancer diagnosis through gas sampling has been shown through canine olfaction, establishing the basis for investigating what biomarker is being detected [21]. Similarly, acetaldehyde is a common metabolite of many bacteria and yeasts, making it a potential marker for detecting infection in bioreactors and food production [22, 23]. While canine olfaction is extremely impressive, this methodology would be challenging to apply in a clinical or industrial setting. As an alternative, a commonly used method, gas chromatography mass spectrometry (GC-MS), is excellent for detecting trace metabolites but suffers from drawbacks like carry-over effects and lack of real-time

measurement [24]. Other gas analysis techniques, like traditional IR spectroscopy, do not offer the sensitivities necessary to detect trace metabolites. Additionally, target biomolecule peaks are convoluted due to broad water peaks in the near-infrared (NIR) and mid-infrared (MIR) regions [25]. Therefore, there is a need to create a novel instrument for the real-time analysis of gas-phase metabolites.

2.1.4 Mid-IR Laser Spectrometry

While measuring acetaldehyde concentrations in the headspace of cell culture media has been previously demonstrated [26, 27]. These studies confirmed the ability to monitor acetaldehyde concentrations ranging from 300 ppb to 1500 ppb. Additionally, in 3D scaffolds, acetaldehyde concentrations as high as 1900 ppb have been measured with selected ion flow tube mass spectrometry (SIFT-MS) [28]. However, these tools cannot provide the real-time analysis needed for bioreactor monitoring in the industry. To alleviate this shortcoming, previous attempts have been made to utilize cryogenically cooled IV-VI semiconductor diode laser technology in combination with absorption spectrometry [29]. Although this study successfully measured acetaldehyde concentrations as low as the 40 ppb range, the requirement of cryogenic cooling places this technology out of the reach of industrial applications. In this study, a novel thermoelectrically-cooled inner cascade laser (ICL) (Nanoplus GmbH) with tunable single-mode tunable emission between 1770.2 cm^{-1} and 1770.4 cm^{-1}, within the R-branch of the carbonyl stretch band, is used to sense acetaldehyde by exciting rotational-vibrational molecular motions within the R-branch of the carbonyl stretch band. The acetaldehyde spectrum exhibits three prominent peaks separated by about 0.020 cm^{-1} from each other. The peak-to-peak voltages for the two strongest peaks at 1770.305 cm^{-1} and 1770.283 cm^{-1} are 291 mV and 212 mV, respectively. Figure 2.2 below shows absorption spectra for a gas sample containing 20 ppm

acetaldehyde in a balance of nitrogen (Specgas, Inc.), lab air, and formic acid headspace plotted as a function of channel number.

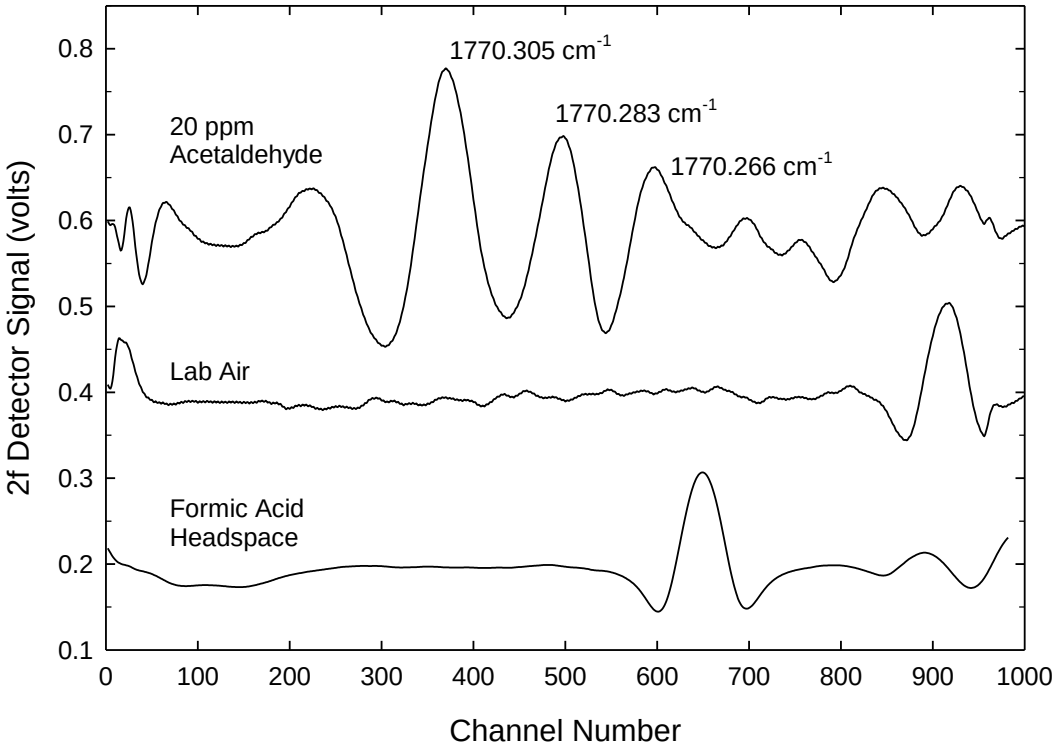

Figure 2.2: Absorption Spectra for Various Headspace Gas Samples

The absorption spectra for various gas headspace samples are plotted as a function of channel number. Second harmonic absorption spectra for laboratory air, formic acid headspace, and 20 ppm acetaldehyde in N_2.

Based on the 20 ppm acetaldehyde calibration spectra in Figure 2.2, the calculated standard deviation for 10 seconds of coadded measured spectra is 0.5 mV, corresponding to a minimum acetaldehyde detection limit of 34 ppb.

2.2 Materials & Methods

2.2.1 Cell Culture

The chosen cell line for this experiment was the EMT6 murine epithelial breast cancer model. All cells were cultured in plates and bioreactors with Waymouth's Medium (Gibco) supplemented with 15% fetal bovine serum (FBS) and 1% antibiotic/antimycotic (Life Technologies) in an incubator at 37°C and 5% CO_2. Before seeding, cells were expanded in T75 cell culture flasks until 80% confluency. They were then lifted with 0.05% trypsin-EDTA (Sigma-Aldrich) and centrifuged at 1100 RCF for 5 minutes to form a cell pellet, the supernatant was discarded, and cells were resuspended at desired concentrations for seeding scaffolds.

2.2.2 PLLA 3D-Printing Filament Production

Due to the chemical additives in commercially available 3D-printing filaments, this study required the production of custom pure PLLA filament. Pure virgin PLLA pellets (NatureWorks LLC; grade 6251D; 1.4% D enantiomer; MW=108,500 kDa) were used in a FilaStruder single screw extruder to produce a 1.75 mm diameter filament. Due to the high melt flow rate of this particular grade PLLA, a metal can with correct guide grooves was used to cool the filament directly upon extrusion to ensure consistent filament diameter.

2.2.3 Hydrogel Scaffold Holding Mesh Production

A custom-designed 3D-printed gel holder mesh was first modeled using Autodesk Fusion360 to prepare the cassette to hold the hydrogel scaffold. The holder mesh was printed using a Creality Ender V2 Neo and a custom-manufactured PLLA filament, as described above. This holder was designed to elevate the gel above the fluid exit and spaced from the chamber's

walls. This allowed unobstructed media flow around the hydrogel scaffold, thus, allowing for the most optimal nutrient diffusion from bulk media. The mesh can be seen in Figure 2.3 below.

Figure 2.3: Hydrogel Scaffold Holding Mesh

The mesh was designed in Autodesk Fusion360 and printed using a Creality Ender 3 V2 Neo. (A): 3D printed mesh inserted into the cassette (B): a 3D rendering of the mesh design (C): the 3D printed mesh before being inserted into the cassette.

2.2.4 Bioreactor Setup and Hydrogel Formation

The bioreactor consisted of 6 individual chambers, one of which is shown as a cross-section in Figure 2.4, each containing a hydrogel scaffold. To achieve fluid flow, the bioreactor utilized a peristaltic pump set at a flow rate of 150µL/min, with silicon tubing (oxygen permeable and impermeable) and at least one media vessel to hold bulk media. Media cycled throughout the bioreactor, entering the chamber's top, flowing around the hydrogel scaffold, and exiting the bottom. For each run, 70 mL of media was used, which cycled throughout the bioreactor ~3 times per day. Depending on the desired media oxygen conditions of the bioreactor, normoxic or variable, the tubing between chambers was run in series (Daisy Chain) or parallel (Figure 2.5). With the bioreactor in the normoxic (parallel) variation, the chambers were plumbed so that each chamber’s inlet was fed directly from the media vessel, and each

chamber's outlet was connected to the input of the media vessel. In the parallel conformation, the oxygen saturation level entering each bioreactor chamber was assumed to be 100% due to the long lengths of oxygen-permeable tubing leading to each chamber. Alternatively, in the Daisy Chain (series) variation, the chambers were plumbed in series such that the outlet of an upstream chamber was connected to the inlet of the chamber immediately downstream using oxygen-impermeable tubing, which prevented the media from reoxygenating, thus lowering the overall media oxygen saturation in a stepwise manner. In this case, the oxygen saturation entering chamber 1 was assumed to be 100% due to the long length of oxygen-permeable tubing leading to chamber 1. The Daisy Chain bioreactor setup allowed the scaffolds to be pushed into simulated hypoxia as far as possible without a hypoxic chamber, which was expected to increase the overall acetaldehyde production of the run. Both bioreactor variations can be seen in Figure 2.5.

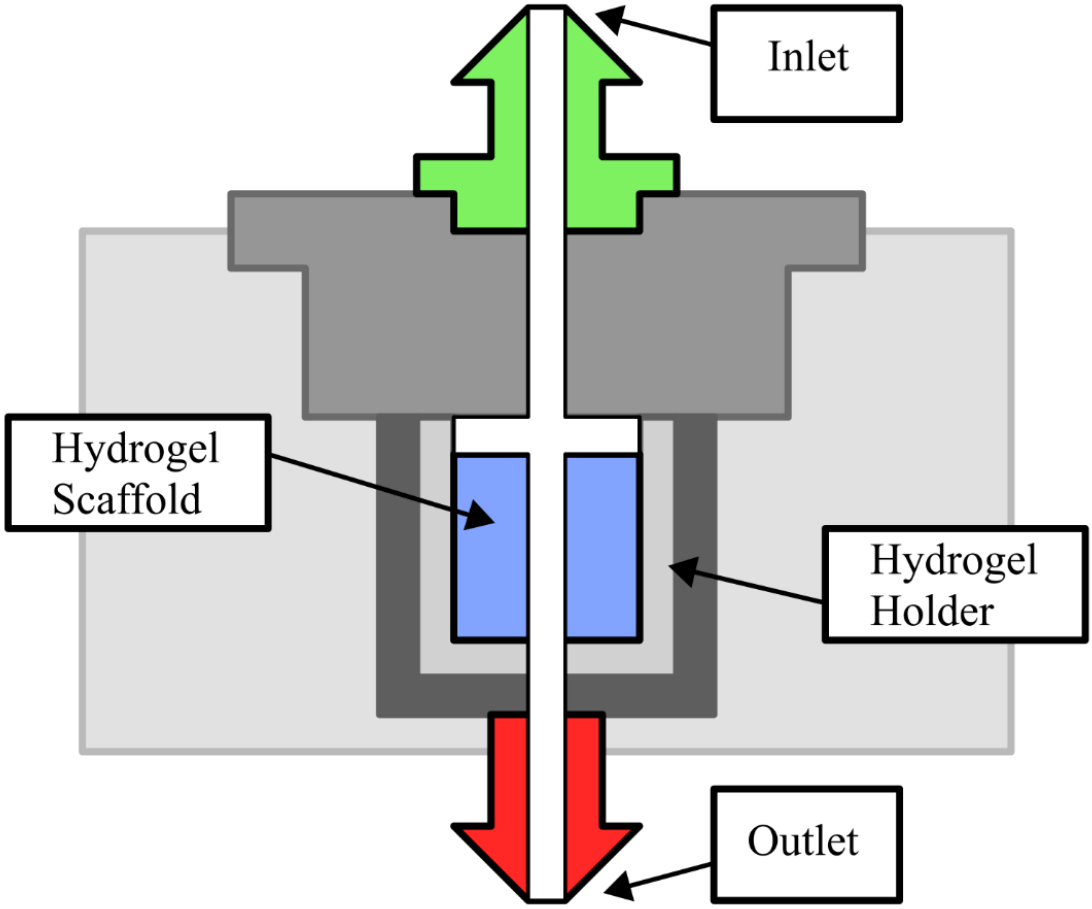

Figure 2.4: Cross-section of a Single Bioreactor Chamber

Cross-sectional diagram of a single chamber in the bioreactor setup, consisting of an inlet, a mesh scaffold holder, a hydrogel scaffold, and an outlet. The media flow surrounds the hydrogel scaffold from all sides, moving from top to bottom.

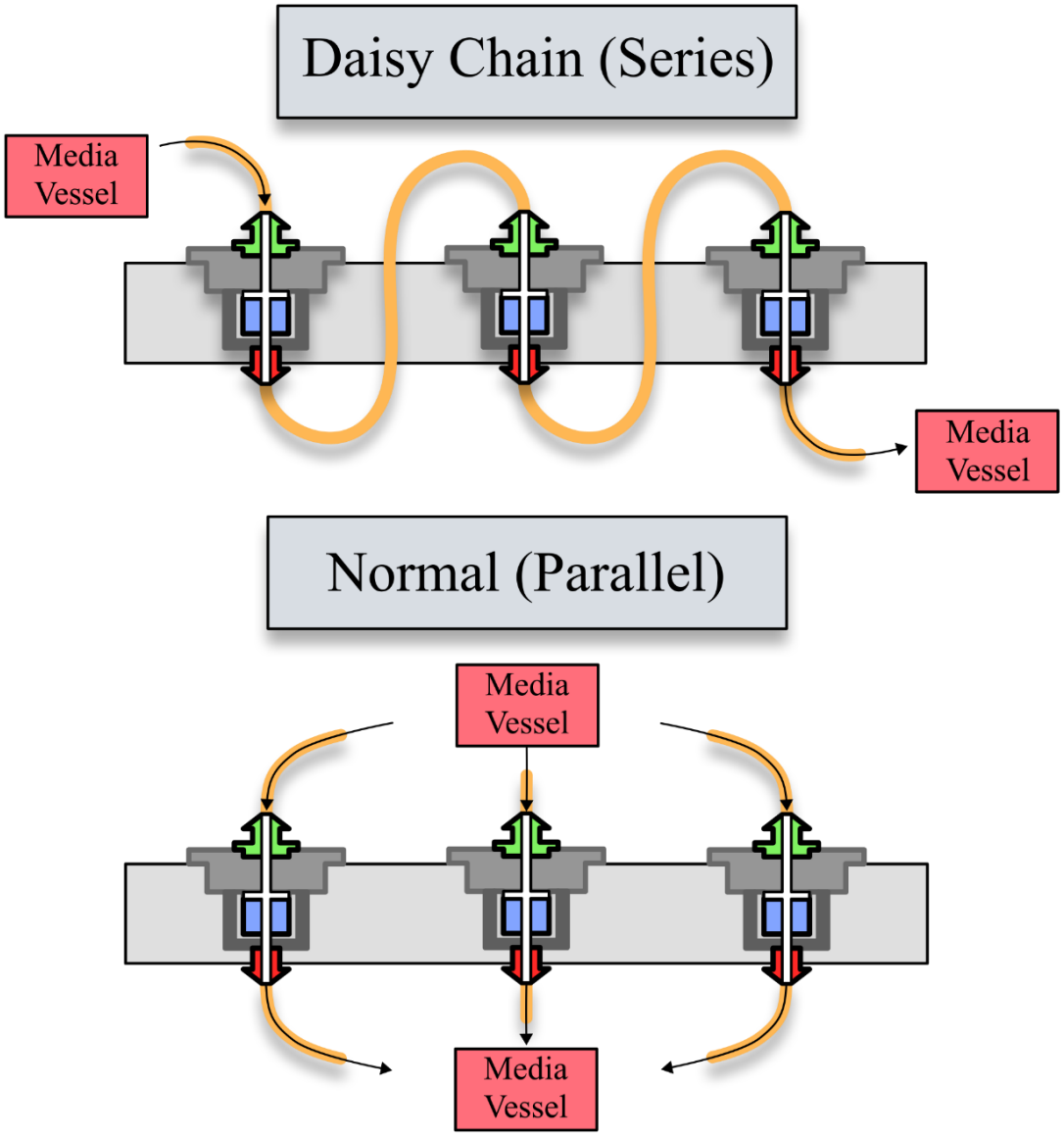

Figure 2.5: Bioreactor Variation Diagram

Diagram of 3 out of 6 bioreactor chambers in the two variations. The Daisy Chain variation (above) is a modification of the bioreactor tubing such that the outlet of each of the six chambers is pumped into the inlet of the next chamber using oxygen-impermeable tubing. This lowered the bulk media oxygen concentration stepwise as the media flowed through each chamber and into the next in series. The typical variation (below) runs the media parallelly, so the media flows through one chamber, is returned to the media vessel, and is reoxygenated. This variation simulates normoxic conditions where the incoming media is fully saturated with oxygen.

Most bioreactor components were sterilized by autoclaving; however, other polymer components were sterilized by ethylene oxide (Anprolene 74i). Autoclavable components were autoclaved on the same day as set up and stored in a sterile hood until use. Gas-sterilized components were run in a 12-hour cycle and stored in a fume hood for at least three days to outgas excess ethylene oxide. The bioreactor was set up before seeding and hydrogel formation to purge the air from the system and allow the cell culture media (Waymouth's) to equilibrate with incubator conditions (37°C, 5% CO_2). The assembled bioreactor and media were placed in the incubator for at least 4 hours before seeding. To prepare cells for seeding in the collagen hydrogel, cells were lifted using 0.05% trypsin-EDTA (Sigma-Aldrich) and centrifuged at 1100 RCF for 5 minutes to create a cell pellet. The supernatant was discarded, and cells were resuspended in a concentration ten times that of the final desired seeding concentration. To prepare the RatCol (Advanced Biomatrix) rat tail type I collagen hydrogel, the included neutralizer solution was mixed with the collagen hydrogel solution in a 1:9 ratio per the manufacturer's instruction, resulting in a 4 mg/mL collagen concentration. The high collagen concentration forms a firm enough gel to resist damage from fluid flow in the bioreactor. Then, for each chamber, 0.4 mL of neutralized collagen solution was mixed with 0.1 mL of cell suspension and pipetted up and down thoroughly. This allowed the cells to be evenly distributed and avoid forming spheroids/clumps too early in the culture. The seeded hydrogel solution was pipetted at 0.5 mL per well in 6 wells of a 96-well plate. The collagen hydrogel was then incubated at 37°C and 5% CO_2 for 1 hour until firm. Once firm, the collagen hydrogel scaffolds were added to the bioreactor by carefully transferring with tweezers onto the custom-designed mesh scaffold holders. The bioreactor was closed, moved back to the incubator, and the media flow rate was set at 150 μL/min. Each bioreactor run lasted 4 days, and media samples from the

media vessels were collected and frozen to preserve volatile metabolites in the liquid phase. These samples were then analyzed with the Mid-IR laser spectrometer to detect acetaldehyde in the headspace or gas phase as a combination of all 6 bioreactor chambers.

2.2.5 Cellularity Quantification

At the 4-day mark, bioreactor runs were stopped, and the number of cells was quantified for each chamber/hydrogel in the bioreactor. To do so, the collagen hydrogel scaffolds were transferred to a 24-well plate and digested in 3 mL of 0.25% (w/v) collagenase type I in unsupplemented Waymouth's Medium for 2 hours. Once fully digested, the media was moved to a 15 mL falcon tube, and wells were washed with another 2 mL of fresh media. The washing media was also added to the 15 mL falcon tube. A 100 µL cell sample of this solution was stained with Trypan Blue (0.4% in Solution; Sigma) and counted using a hemocytometer.

2.2.6 Acetaldehyde Measurement

The procedure for acetaldehyde measurement is located in Appendix section A1.1.

2.3 Results

2.3.1 Bioreactor Cell Growth

Total bioreactor cellularity (6 chambers) was quantified per run and displayed as initial seeding and final cell quantities in Figure 2.6. The total percent growth of all bioreactor runs, including variable and normoxic, were organized based on initial seeding cell quantities and displayed as individual bars per run in Figure 2.7. While at lower seeding quantities, the percent growth for both normoxic (parallel) and Daisy Chain (series) runs are similar, in the case of the variable oxygen condition runs, a more gradual decrease in percent growth is demonstrated as

seeding cell quantity increases. Additionally, these runs showed higher cell growth regardless of seeding quantities, whereas normoxic (parallel) variation runs demonstrated a plateau in percent growth as seeding concentrations increased (Figure 2.7).

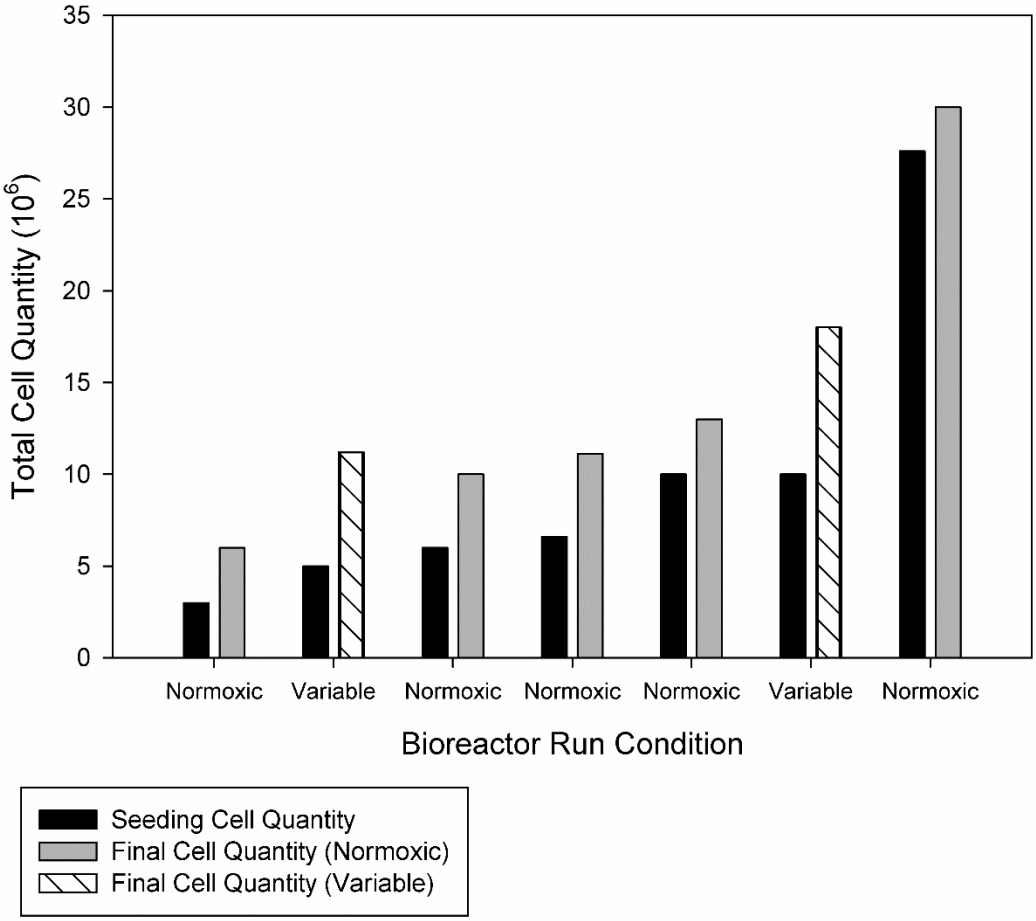

Figure 2.6: Total Seeding and Final Cell Quantity for Consecutive Bioreactor Runs

Cell Quantity is reported as a total of all six bioreactor chambers. Daisy Chain (series) setup, or runs where bulk media dissolved oxygen concentration surrounding hydrogel scaffolds varies as the media flows downstream in the series of chambers, are highlighted in white with diagonal hashes.

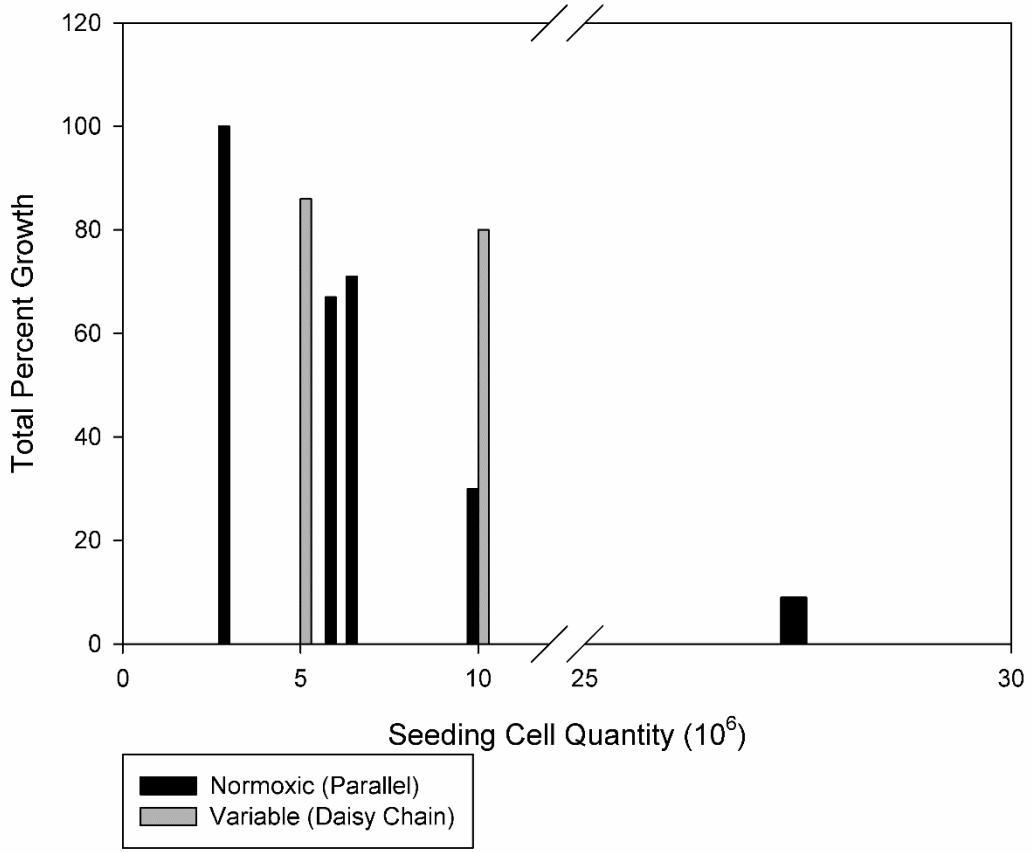

Figure 2.7: Total Percent Growth of Bioreactor Run vs. Seeding Cell Quantity

Percent growth is reported as a function of the total cellularity of all six bioreactor chambers and is the percent change from total seeding to total final cell quantity. Daisy Chain (series) setup, or runs where bulk media dissolved oxygen concentration surrounding hydrogel scaffolds varies as the media flows downstream in the series of chambers, are highlighted in white with diagonal hashes. Generally, runs with higher seeding cell quantities and variable hypoxia displayed higher growth percentages than their normoxic counterparts.

2.3.2 Acetaldehyde Measurements

Bulk media headspace gas-phase acetaldehyde concentrations after 4 days are listed in Table 2.1 on a per-run basis. The bulk media headspace gas-phase acetaldehyde concentration in normoxic (parallel) runs decreases as the seeding cell quantity increases. In contrast, this trend

seems reversed in Daisy Chain (series) runs seen in Figure 2.8. The total acetaldehyde production per cell was calculated and plotted against the total percent growth to more accurately compare acetaldehyde levels between runs with different cell quantities. This plot tended to increase with higher total percent growth (Figure 2.9).

Table 2.2: Bulk Media Headspace Gas-phase Acetaldehyde Concentrations and Bioreactor Run Conditions

Bulk media headspace gas-phase acetaldehyde concentrations were measured using Mid-IR laser spectrometry. Bioreactor run number, seeding and final cell quantity, total percent growth, conformation, and bulk media headspace gas-phsae acetaldehyde concentration are listed per run.

	Cell Quantity (10^6)				**Acetaldehyde Measurement**
Run	**Seeded**	**Finished**	**Total Percent Growth**	**Conformation**	**Avg ppm**
1	3	6	100%	Normoxic	0.783
2	6	10	67%	Normoxic	0.974
3	6.6	11.3	71%	Normoxic	0.740
4	10	13	30%	Normoxic	0.205
5	27.6	30	9%	Normoxic	0.315
6	5	9.3	86%	Daisy Chain	0.708
7	10	18	80%	Daisy Chain	1.547

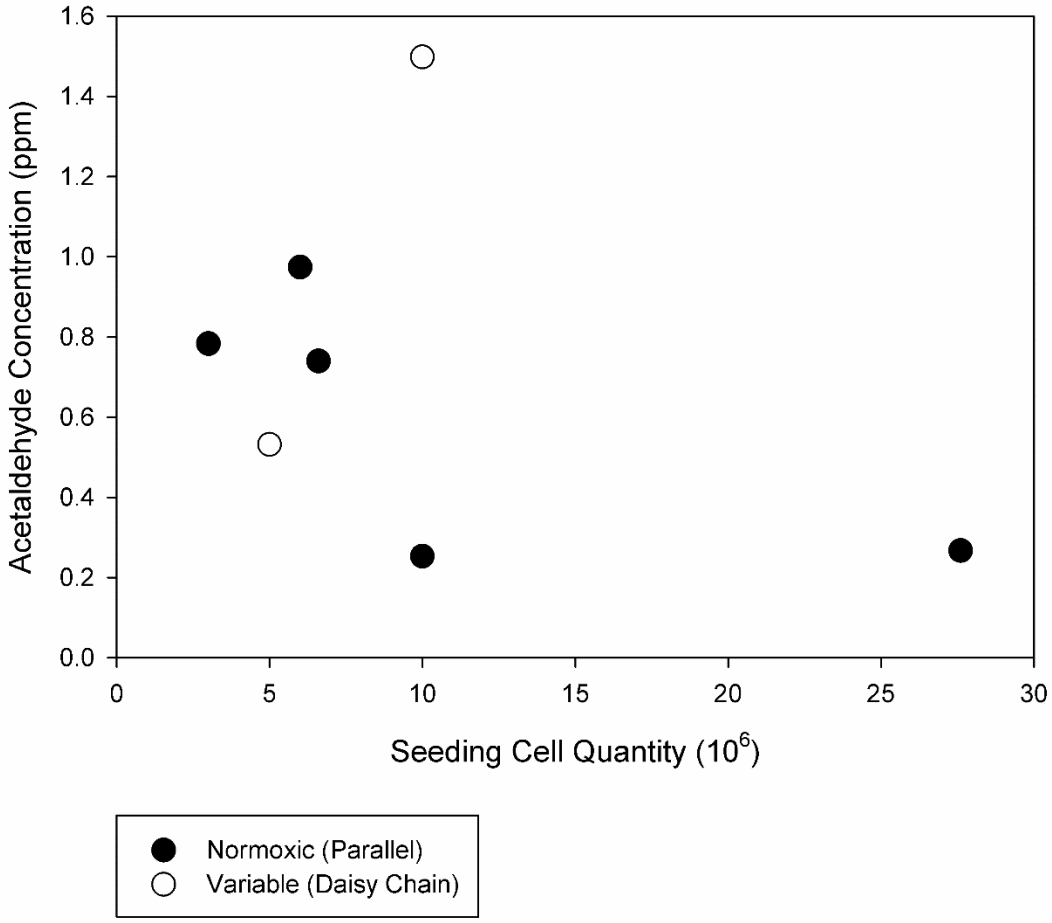

Figure 2.8: Gas-phase Acetaldehyde Concentration vs. Bioreactor Seeding Cell Quantity
Bulk media acetaldehyde concentrations are reported in ppm and seeding cell quantity in 10^6 cells. Acetaldehyde concentration in bioreactor runs with normoxic (parallel) chamber setup showed a trend of decreasing concentration as cell number increases. However, bioreactor runs performed with the Daisy Chain (series) or runs where bulk media dissolved oxygen concentration surrounding hydrogel scaffolds varies as the media flows downstream in the series of chambers, represented with empty circles and a dotted line, showed a trend in increasing acetaldehyde concentrations as cell quantity increased.

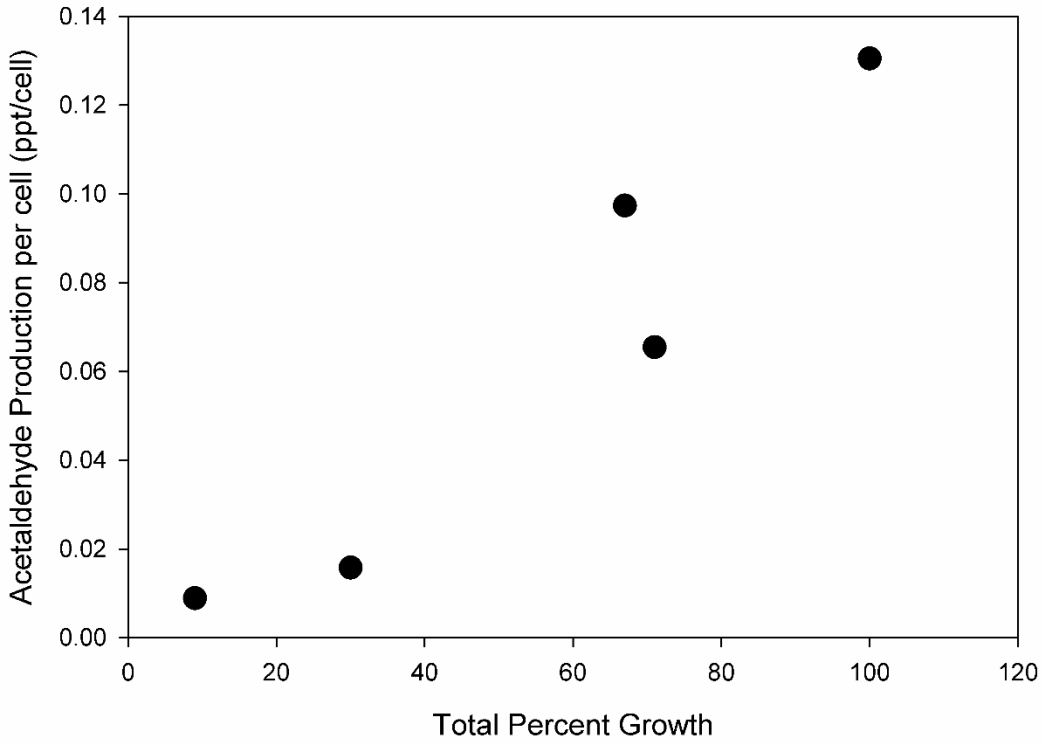

Figure 2.9: Gas-phase Acetaldehyde Production per cell vs. Total Percent Growth in Normoxic Runs

Acetaldehyde production is reported in ppt/cell, which was calculated as $\frac{\textbf{total acetaldehyde prod}}{\textbf{number of cells}}$.

Total percent growth is a function of the final total cellularity of all six bioreactor chambers and is the percent change from total seeding to total final cell quantity. Acetaldehyde production per cell in bioreactor runs with a normoxic (parallel) chamber setup showed a trend of increasing and peaking as total percent growth increases.

Figure 2.10 plots the average acetaldehyde production per cell versus the seeding cell quantity for each bioreactor run. This plot shows a steep drop in per-cell acetaldehyde production as seeding cell quantity increases in normoxic (parallel) runs. However, in Daisy Chain (series) runs, this trend is reversed at higher seeding quantities per-cell acetaldehyde production increases as seeding cell quantity increases.

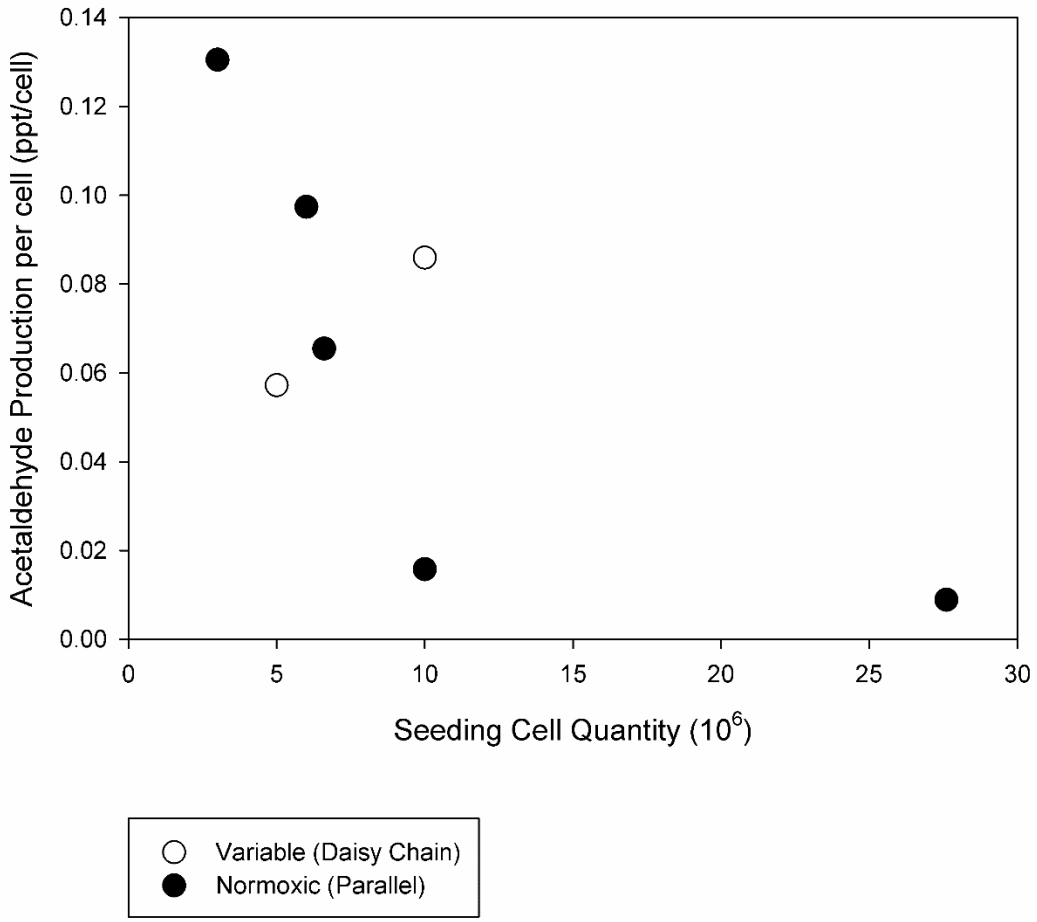

Figure 2.10: Acetaldehyde Production per Cell vs. Seeding Cell Quantity by Run
Acetaldehyde production is reported per cell in ppt/cell. The calculation is based on the final total cellularity. Daisy Chain (series) setup, or runs where bulk media dissolved oxygen concentration surrounding hydrogel scaffolds varies as the media flows downstream in the series of chambers, are highlighted with empty circles and a dotted line. Variable oxygen runs demonstrated a trend of increasing production per cell as seeding cell quantity increased. Conversely, normoxic (parallel) runs demonstrated a per-cell decrease as seeding cell quantity increased.

2.4 Discussion

Positive total growth percentages were recorded regardless of Daisy Chain (series) or normoxic (parallel) run variation. Figures 2.6, 2.7, and Table 2.1 all display the positive total

growth percentages, a function of the total cellularity of all six bioreactor chambers, in each bioreactor run. The lowest growth percentage was found in run number 5 at 9% and the highest in run 1 at 100% (Table 2.1). The disparity is likely due to spacial and diffusional limitations within the hydrogel scaffold. In essence, the total maximum capacity of the bioreactor was likely approached during run five due to such a high seeding cell quantity. This effect is also conversely demonstrated in runs 1, 2, and 3. Due to these runs' relatively lower seeding cell quantities, the cells could expand without spacial or nutrient-diffusional limitations, with each of these runs showing a total percent growth of at least 67%. Introducing the variable media oxygen saturation conditions in the Daisy Chain (series) bioreactor setup appeared to change the behavior of the cells, such that regardless of the seeding cell quantity, the cells could proliferate at a greater rate. This effect was more noticeable at higher seeding quantities, specifically when comparing runs 4 and 7, which were both seeded with 10 million cells. Run 7 was done with the Daisy Chain (series) variation, with a total percent growth of 80%. In contrast, run 4 was done with the normoxic (parallel) variation and had a much lower percent growth of 30%, displayed in Figure 2.7. This shift in behavior could be a shift in metabolism, favoring the glycolytic pathway rather than OXPHOS, thus creating more synthesis-focused cellular components, as described in Figure 2.1. Regardless of bioreactor variation, the modified flow-perfusion system successfully accommodated the chosen EMT6 cell line, and potentially other cell lines, proving to be a promising *in vitro* cancer testing model. Additionally, by changing the variation of the bioreactor system, we successfully changed the behavior of the cells, likely due to simulated variable oxygen tensions in the hydrogels, to more closely mimic the physiology of solid tumors.

Once the bioreactor variations were confirmed as viable test beds for cancer cells, media headspace gas-phase acetaldehyde measurements could be taken. These measurements are shown

in Table 2.1. The measurements differed between the two bioreactor variations, with the highest normoxic (parallel) run concentration at 0.974 ppm and the highest Daisy Chain (series) run concentration at 1.547 ppm. The acetaldehyde concentration also depended on the seeding cell quantity in normoxic conditions. Generally, the acetaldehyde concentration in the headspace of used media peaks at around 6 million cells and decreases as the seeding cell quantity increases (Figure 2.8). This is most likely linked to the lower total percent growth as the seeding cell quantity increases. Figure 2.9 shows the increasing acetaldehyde production per cell as total percent growth increases. A possible explanation for this observation could be that cells with a synthesis-focused metabolism tend to produce more acetaldehyde due to the shift to a glycolytic phenotype required for synthesizing cellular components needed for cell division. This again signals back to the Warburg metabolism, signified by a build-up of pyruvate and synthesis components in the cytosol. Additionally, bioreactor runs with the Daisy Chain (series) variation exhibited higher acetaldehyde production per cell than normoxic (parallel) bioreactor runs. This is exaggerated with higher seeding quantities. Again, runs 4 and 7, which were both seeded at 10 million cells, are excellent examples of this behavior. Similar to total growth percentage, runs 4 and 7 exhibit different headspace gas-phase acetaldehyde total concentrations (Figure 2.8), 0.205 ppm and 1.547 ppm, respectively, and per-cell acetaldehyde production (Figure 2.10), 0.0158 ppt/cell and 0.0859 ppt/cell respectively. This trend agrees with the previously proposed explanation for the discrepancies in total percent growth, that the variable oxygen conditions could push the cells to exhibit a predominantly glycolytic phenotype, thus generating more pyruvate build-up, which then decomposes to acetaldehyde. Nonetheless, the newly proposed mid-IR laser spectrometer could accurately detect acetaldehyde concentrations as low as ~200 ppb (Table 2.1). This technology also provides more capabilities when compared to currently

utilized gas-phase metabolite analytical tools, such as GC-MS. Mid-IR spectrometry offers the ability of real-time measurement in sub-ppm ranges, establishing the possibility for its use in many industrial applications.

2.5 Conclusion

This study aimed to modify the flow-perfusion bioreactor to create an *in vitro* solid tumor model for analyzing gas-phase metabolites. Adding a 3D collagen hydrogel scaffold and a custom-designed 3D-printed mesh hydrogel holder to the bioreactor enabled the use of the EMT6 cancer cell line as a potential solid breast tumor model. This modification has shown promise, as total percent growth was positive for each bioreactor run. Additionally, utilizing the bioreactor in the Daisy Chain (series) variation can influence the model's behavior by inducing variable media oxygen concentration and, thus, partial hypoxia. The change in cell behavior indicated a potential transition to a higher expression of a Warburg metabolic phenotype. Once this model was proven viable for cell growth, it could be used as a testing platform to validate the practicality of utilizing mid-IR laser spectrometry as a gas-phase metabolite analysis tool. While many volatile gas-phase metabolites exist, like ethanol and pyridine, acetaldehyde was chosen as a potential biomarker for cancer due to its exothermic production from pyruvate and the suspected elevation of pyruvate concentrations in cancer cells. The used mid-IR laser spectrometer measured acetaldehyde concentrations as low as ~200 ppb and, in theory, should be able to measure concentrations as low as 34 ppb. Comparing the acetaldehyde production per cell in normoxic (parallel) bioreactor runs with the total percent growth showed a positive trend, increasing with higher levels of total percent growth. Additionally, when the bioreactor was used in the Daisy Chain (series) variation, the acetaldehyde production per cell increased as the seeding cell quantity increased, which was reversed in the normoxic (parallel) bioreactor runs.

This could indicate higher pyruvate accumulation in more hypoxic conditions, which agrees with a shift towards a glycolytic phenotype. These findings lend promise to using mid-IR laser spectrometry as a potential gas-phase monitoring technique.

Moving forward, this technology should be adapted to analyze real-time bioreactor metabolites, which could lend itself well to working with artificial intelligence for data interpretation and culture data prediction. Additionally, the effects of hypoxia on cell metabolism should be further explored to understand how this would impact the *in vitro* solid tumor model.

2.6 Acknowledgments

I acknowledge the following collaborators: Dr. Patrick McCann and Khosrow Namjou. I would also like to acknowledge support from the Oklahoma Center for the Advancement of Science and Technology (OCAST).

2.7 References

[1] O. Warburg, "Tests on surviving Carcinoma cultures.," (in German), *Biochemische Zeitschrift,* vol. 142, pp. 317-333, 1923 1923.

[2] P. Vaupel, H. Schmidberger, and A. Mayer, "The Warburg effect: essential part of metabolic reprogramming and central contributor to cancer progression," *International Journal of Radiation Biology,* vol. 95, no. 7, pp. 912-919, 2019-07-03 2019, doi: 10.1080/09553002.2019.1589653.

[3] P. Vaupel and G. Multhoff, "Revisiting the Warburg effect: historical dogma *versus* current understanding," *The Journal of Physiology,* vol. 599, no. 6, pp. 1745-1757, 2021, doi: 10.1113/jp278810.

[4] J. Yang, J. Nie, X. Ma, Y. Wei, Y. Peng, and X. Wei, "Targeting PI3K in cancer: mechanisms and advances in clinical trials," *Molecular Cancer,* vol. 18, no. 1, 2019, doi: 10.1186/s12943-019-0954-x.

[5] D. B. Shackelford and R. J. Shaw, "The LKB1–AMPK pathway: metabolism and growth control in tumour suppression," *Nature Reviews Cancer,* vol. 9, no. 8, pp. 563-575, 2009, doi: 10.1038/nrc2676.

[6] R. Courtnay, D. C. Ngo, N. Malik, K. Ververis, S. M. Tortorella, and T. C. Karagiannis, "Cancer metabolism and the Warburg effect: the role of HIF-1 and PI3K," *Molecular Biology Reports,* vol. 42, no. 4, pp. 841-851, 2015, doi: 10.1007/s11033-015-3858-x.

[7] S. Ganapathy-Kanniappan and J.-F. H. Geschwind, "Tumor glycolysis as a target for cancer therapy: progress and prospects," *Molecular Cancer,* vol. 12, no. 1, p. 152, 2013, doi: 10.1186/1476-4598-12-152.

[8] V. L. Payen, E. Mina, V. F. Van Hee, P. E. Porporato, and P. Sonveaux, "Monocarboxylate transporters in cancer," *Molecular Metabolism,* vol. 33, pp. 48-66, Mar 2020, doi: 10.1016/j.molmet.2019.07.006.

[9] P. O'Mara, A. Farrell, J. Bones, and K. Twomey, "Staying alive! Sensors used for monitoring cell health in bioreactors," *Talanta,* vol. 176, pp. 130-139, Jan 2018, doi: 10.1016/j.talanta.2017.07.088.

[10] P. S. Kelly *et al.*, "Improvements in single-use bioreactor film material composition leads to robust and reliable Chinese hamster ovary cell performance," *Biotechnology Progress,* vol. 35, no. 4, 2019, doi: 10.1002/btpr.2824.

[11] M. Paolillo *et al.*, "Stem-Like Cancer Cells in a Dynamic 3D Culture System: A Model to Study Metastatic Cell Adhesion and Anti-Cancer Drugs," (in en), *Cells,* vol. 8, no. 11, p. 1434, 2019/11 2019, doi: 10.3390/cells8111434.

[12] P. Harms, Y. Kostov, and G. Rao, "Bioprocess monitoring," *Current Opinion in Biotechnology,* vol. 13, no. 2, pp. 124-127, Apr 2002, doi: 10.1016/s0958-1669(02)00295-1.

[13] Z. H. Liu, F. L. Luo, and T. L. Chen, "Phenolphthalein immobilized membrane for an optical pH sensor," *Analytica Chimica Acta,* vol. 510, no. 2, pp. 189-194, May 2004, doi: 10.1016/j.aca.2004.01.019.

[14] C. Demuth, J. Varonier, V. Jossen, R. Eibl, and D. Eibl, "Novel probes for pH and dissolved oxygen measurements in cultivations from millilitre to benchtop scale," *Applied Microbiology and Biotechnology,* vol. 100, no. 9, pp. 3853-3863, 2016, doi: 10.1007/s00253-016-7412-0.

[15] Y. Zhao, H. Zhang, Q. Jin, D. Jia, and T. Liu, "Ratiometric Optical Fiber Dissolved Oxygen Sensor Based on Fluorescence Quenching Principle," *Sensors,* vol. 22, no. 13, p. 4811, 2022, doi: 10.3390/s22134811.

[16] H.-Y. Goh, M. Sulu, H. Alosert, G. L. Lewis, G. D. Josland, and D. E. Merriman, "Applications of off-gas mass spectrometry in fed-batch mammalian cell culture," *Bioprocess and Biosystems Engineering,* vol. 43, no. 3, pp. 483-493, 2020, doi: 10.1007/s00449-019-02242-2.

[17] M. Takahashi, Y. Sawada, and H. Aoyagi, "Erratum to: Development of a circulation direct sampling and monitoring system for O2 and CO2 concentrations in the gas–liquid

phases of shake-flask systems during microbial cell culture," *AMB Express,* vol. 7, no. 1, 2017, doi: 10.1186/s13568-017-0481-3.

[18] W. Filipiak, K. Jaroch, P. Szeliska, K. Żuchowska, and B. Bojko, "Application of Thin-Film Microextraction to Analyze Volatile Metabolites in A549 Cancer Cells," *Metabolites,* vol. 11, no. 10, p. 704, 2021, doi: 10.3390/metabo11100704.

[19] R. A. Alberty, "Thermodynamics in Biochemistry," in *Encyclopedia of Life Sciences*.

[20] CHERIC. Pure Component Properties

[21] C. Guest *et al.*, "Feasibility of integrating canine olfaction with chemical and microbial profiling of urine to detect lethal prostate cancer," *PLOS ONE,* vol. 16, no. 2, p. e0245530, 2021, doi: 10.1371/journal.pone.0245530.

[22] S. B. Raj, S. Ramaswamy, and B. V. Plapp, "Yeast Alcohol Dehydrogenase Structure and Catalysis," *Biochemistry,* vol. 53, no. 36, pp. 5791-5803, 2014, doi: 10.1021/bi5006442.

[23] A. Yokoi *et al.*, "Relationship between acetaldehyde concentration in mouth air and characteristics of microbiota of tongue dorsum in Japanese healthy adults: a cross-sectional study," *Journal of Applied Oral Science,* vol. 27, 2019, doi: 10.1590/1678-7757-2018-0635.

[24] O. Fiehn, "Metabolomics by Gas Chromatography–Mass Spectrometry: Combined Targeted and Untargeted Profiling," *Current Protocols in Molecular Biology,* vol. 114, no. 1, 2016, doi: 10.1002/0471142727.mb3004s114.

[25] A. A. Bunaciu, V. D. Hoang, and H. Y. Aboul-Enein, "Applications of FT-IR Spectrophotometry in Cancer Diagnostics," *Critical Reviews in Analytical Chemistry,* vol. 45, no. 2, pp. 156-165, 2015, doi: 10.1080/10408347.2014.904733.

[26] H.-W. Shin *et al.*, "Acetaldehyde and hexanaldehyde from cultured white cells," *Journal of Translational Medicine,* vol. 7, no. 1, p. 31, 2009, doi: 10.1186/1479-5876-7-31.

[27] C. Heit, P. Eriksson, D. C. Thompson, G. Charkoftaki, K. S. Fritz, and V. Vasiliou, "Quantification of Neural Ethanol and Acetaldehyde Using Headspace GC-MS," *Alcoholism: Clinical and Experimental Research,* vol. 40, no. 9, pp. 1825-1831, 2016, doi: 10.1111/acer.13156.

[28] A. V. Rutter, T. W. E. Chippendale, Y. Yang, P. Španěl, D. Smith, and J. Sulé-Suso, "Quantification by SIFT-MS of acetaldehyde released by lung cells in a 3D model," *The Analyst,* vol. 138, no. 1, pp. 91-95, 2013, doi: 10.1039/c2an36185j.

[29] P. C. Kamat *et al.*, "Measurement of acetaldehyde in exhaled breath using a laser absorption spectrometer," *Applied Optics,* vol. 46, no. 19, pp. 3969-3975, Jul 2007, doi: 10.1364/ao.46.003969.

3. Effects of Hypoxia on EMT6 Cancer Cells in a Perfusion Bioreactor 3D Hydrogel Tumor Model

Abstract

Cancer research has been and will continue to be a mainstay globally, thus solidifying the need for better *in vitro* testing models. Current in vitro models commonly rely on 2D monolayer cell culture techniques, which are outdated and ill-representative of physiological tissues. Additionally, the studies employing 3D in vitro models lack the critical flow component in physiological tissues. While microfluidics is becoming more popular, this technique lacks the scale to recapitulate prominent solid tumor pathophysiological characteristics, like diffusion of nutrients, elevated interstitial fluid pressure, and use of cocultures. This study proposes using a modified flow-perfusion bioreactor combined with 3D collagen hydrogel scaffolds as a solid tumor model that includes more characteristics found in vivo. Furthermore, bioreactor tubing was connected such that variable levels of media oxygen saturation were generated. The step-wise oxygen saturation drop was created by connecting each bioreactor chamber in a series without allowing for media reoxygenation in a configuration dubbed the "Daisy Chain." This configuration created artificial hypoxia within each scaffold, a major variable in the diagnosis and treatment of solid tumors. The bioreactor was paired with previously used custom-designed optical oxygen sensors to confirm the expected step-wise drop in media oxygen saturation. In doing so, it was determined that the oxygen uptake rate per cell for cells in the normoxic region, even in decreased oxygen saturation conditions, was consistent throughout the run, indicating almost no change in metabolism. Cell proliferation and viability were assessed to determine the validity and effects of the estimated increased downstream hypoxia. These measurements

confirmed the expected increase in hypoxic core volume by showing decreased cell proliferation and viability in downstream chambers. Finally, a modified spheroid hypoxia model was applied using empirically measured data for our hydrogel and the EMT6 cell line to estimate the depth into each scaffold until oxygen concentrations are lowered to hypoxic levels. The model confirmed our findings and predicted a larger hypoxic region in downstream scaffolds.

3.1 Introduction

3.1.1 Pathophysiology and Microenvironment of Solid Tumors

Solid tumors function similarly to natural tissues, requiring adequate blood flow to supply nutrients and remove waste. The problem arises when these tumors quickly outgrow host blood vessels. As this occurs, the cancer cells stimulate new vessel growth, a process known as angiogenesis. The newly formed tumor vasculature is primitive and disorganized compared to the host vasculature [1]. These tumor vessels are “leaky” and cannot correctly deliver nutrients and oxygen to the tumor. As such, cancer cells within the tumor are nutrient-deprived and oxygen-starved. Environmental conditions within tumors are harsh, yet most of the deprived cells are still viable. As a result of these conditions, cancer cells are often resistant to many different forms of treatment due to abnormalities in genetic expression and reprogramming of the immune system [2].

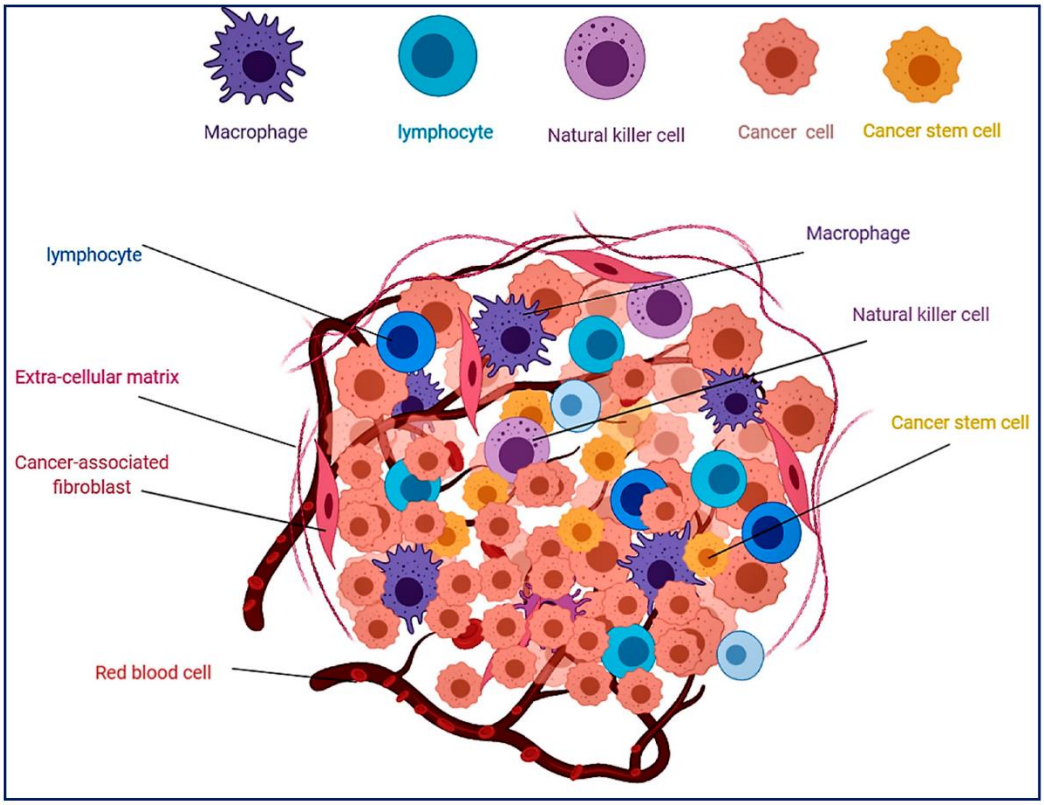

Figure 3.1: Solid Tumor Diagram Exhibiting Multiple Cell Types

Illustration of solid tumor and its microenvironment showing the multiple different cell phenotypes present. The figure was used with permission from the following publication [3].

Some notable characteristics in solid tumor pathophysiology include high interstitial fluid pressure, glycolytic metabolism, acidic pH, and hypoxia [1, 4]. The interstitial fluid pressure (IFP) of tumors is generally heterogeneous and elevated due to immature vasculature and lymphatic abnormalities. Elevated IFP has been investigated as a potential biomarker for cancer and has been correlated with lower survival rates [4-6]. This also poses a potential problem for drug delivery to tumors since elevated IFP can limit the ability of drugs to disperse in tumors by convection [7]. In addition, the tumor microenvironment exhibits an acidic pH due the excessive lactic acid production. This is due to the overexpressed glycolytic metabolism in cancer cells, as previously described in section 2.1.1. The hypoxic nature of the tumor further exaggerates a

glycolytic metabolism. While all these factors together make up the tumor pathophysiology, the hypoxic nature of solid tumors has been the most investigated and will be explored further in depth in section 3.1.2.

One central element that shapes the tumor microenvironment is the interaction between the cancer cells and the immune system, specifically the immune cells. Of these immune cells, the most prevalent include macrophages, natural killer (NK) cells, and lymphocytes [3]. It has been difficult to fully understand the interactions between tumors and the immune system, primarily due to the conflicting reports of immune cells' roles in this interaction [8-10]. However, it is understood that these cells can be necessary for the survival of tumors and serve as biomarkers. Macrophages are commonly found in the tumor microenvironment and have been shown to promote cancer progression and metastasis by creating a stroma conducive to neoplastic invasion [11]. For example, macrophages with the M2 phenotype can be activated by IL-4 produced by cancer cells, and in return, the macrophages supply the tumor with epidermal growth factor (EGF), promoting cancer migration [12, 13]. Additionally, these macrophages can provide matrix-degrading enzymes such as metalloproteinases and cysteine cathepsin proteases, which allow cancer cells to migrate throughout the extracellular matrix (ECM) more efficiently [11]. Macrophages are not the only immune cell responsible for cancer progression. T lymphocytes, specifically regulatory CD4+ T-cells, can promote immune evasion by silencing activated CD8+ T-cells. This is done through multiple mechanisms, but the most prevalent are immune checkpoint molecules, such as programmed cell death 1 (PD-1) and cytotoxic T-lymphocyte-associated protein 4 (CTLA-4) [14]. Activated CD8+ T-cells can also become exhausted due to prolonged antigen exposure and overexpression of these immune checkpoint inhibitors [8].

While not a type of immune cell, cancer-associated fibroblasts (CAFs) have been associated with the stage and progression of tumors. In healthy tissues, fibroblasts are key in ECM remodeling and synthesis during wound healing and become activated by tissue damage [15]. The origin of CAFs can vary, but regardless of origin, these cells can contribute to the growth and survival of tumors through several different mechanisms. The prime example is the hijacking of these CAFs by adjacent cancer cells to create tumor ECM components [15]. CAFs can also provide immune suppression to cancer cells through the excretion of transforming growth factor (TGF)-β, IL-4, and vascular endothelial growth factor (VEGF) [15, 16]. Understanding the pathophysiology and microenvironment of solid tumors is key to creating accurate *in vitro* models. While the proposed model does not consider the effects of immune or stromal cells, it does include 3D ECM components, which is a step towards improving upon the commonly used 2D monolayer *in vitro* models. The 3D nature of the model imposes more accurate physiological restrictions upon the cells (diffusion, migration, etc.). Combined with the flow-perfusion bioreactor, this model can more accurately represent *in vivo* nutrient delivery.

3.1.2 Significance of Hypoxia in Cancer

Hypoxia is the most investigated of all regularly cited solid tumor pathophysiological characteristics due to its commonality in solid tumors. Hypoxia is defined as oxygen tensions less than 10 mmHg and is generally caused by insufficient oxygen supply from immature, poorly formed vasculature. Many hypoxia studies revolve around understanding the hypoxia-inducible factors (HIFs). HIFs are heterodimers, consisting of an oxygen-sensitive α-subunit and a constitutively expressed β-subunit. In normoxic conditions, the α-subunit is marked for degradation by HIF prolyl hydroxylase domain family proteins (PHDs), which utilize O_2 as a substrate. Intracellular O_2 levels largely regulate the PHDs, and when this level drops PHDs no

longer mark HIF-α for degradation [17, 18]. The stable α-subunit can then enter the nucleus and dimerize with the HIF-β subunit, which binds to the hypoxia response elements (HREs) on target genes, increasing RNA expression [18, 19]. HIFs also play a role in the immunosuppressive properties of the tumor microenvironment. The hypoxic tumor environment can recruit myeloid-derived suppressor cells (MDSCs) as well as upregulate the expression of immune checkpoint ligands like programmed death ligand-1 (PD-L1) in these cells [20, 21]. Additionally, the lowered oxygen concentrations can reduce the effectiveness of invading immune cells like CD4+ T cells, CD8+ T cells, and NK cells [21]. Cancer cell metabolism is also affected by HIFs. Through the upregulation of pyruvate dehydrogenase kinase 1 (PDK-1) and lactate dehydrogenase A (LDH-A), pyruvate is blocked from entering mitochondria and instead converted to lactic acid [18]. Hypoxia has also been related to cancer drug resistance. For example, HIFs have also been linked to the overexpression of multidrug transport P-gp, encoded by the MDR1 gene, resulting in more drug-efflux proteins.

Due to the importance of hypoxia in studying cancer, it is apparent that a valid *in vitro* model must incorporate this effect to represent *in vivo* responses accurately. This study modified the flow-perfusion bioreactor to recapitulate *in vivo* tumors by decreasing oxygen tensions in the 3D hydrogel scaffolds. Further analysis was performed using optical oxygen sensors. Additionally, empirically measured data was used to modify a spheroid oxygen tension model, which was then used to estimate the size of the hypoxic core in each 3D hydrogel scaffold.

3.2 Materials & Methods

3.2.1 Cell Culture

The cell culture procedure was followed the same as previously described in section 2.2.1.

3.2.2 Bioreactor Setup and Hydrogel Formation

The bioreactor setup procedure was followed as previously described for the Daisy Chain variation in section 2.2.3. This procedure was modified to include the optical oxygen sensors after chambers 3 and 6. Each scaffold in the bioreactor was seeded with 770,000 cells for a total seeding quantity of 4.6 million cells.

3.2.3 Oxygen Data Collection

The oxygen sensors utilized the RedEye oxygen sensing patches (Ocean Optics). These patches were contained within an oxygen sensing module (OxyMod), developed initially by Simmons [22]. The main body of the utilized oxygen sensors consisted of square glass tubing to which the RedEye patch was attached. The glass tubing then had a custom-designed 3D-printed housing fitted around the tubing to block excess light and act as a guide for the probe. Finally, barbed tubing fittings were epoxied to the ends to seal the sensors. The optical oxygen-sensing patches contained two fluorescent molecules, ruthenium and Pt-porphyrin complexes [23]. The fluorescent emission of this material is directly related to the media oxygen saturation by the Stern-Volmer equation [23]. These sensors were paired with the NeoFox Viewing System (Ocean Optics) to determine relative oxygen saturations within the media. The NeoFox Viewing System used a fiber optic probe that pulsed blue light at 450 nm to excite the fluorescent material. The same probe then captured the fluoresced light. This data was passed to the NeoFox Viewer

software and related to the media oxygen saturation level. The oxygen saturation levels ranged from 0 to 100%, where 100% was the maximum oxygen saturation for media in the given environmental conditions (37°C, 5% CO_2). The partial pressure of O_2 for the 100% relative saturation value was calculated using the environmental conditions of 1 atm, 95% relative humidity, 5% CO_2, and 21% O_2. This partial pressure was then used to calculate the dissolved O_2 concentration in the liquid by Henry's Law. The Henry's Law constant (K) was calculated using the Van't Hoff equation to adjust for the higher incubator temperature. The utilized K at 37°C of 1.04 mmol/L/atm was calculated from the value provided by Sander et al. of 1.3 mmol/L/atm at 25°C [24]. The concentration of dissolved O_2 was assumed to be 0 at 0% saturation. Using these concentration values, a linear equation relating the relative percent saturation levels to dissolved O2 concentrations can be created (Figure A2.3).

The media entering chamber 1 was previously shown to be 100% saturated, so only exiting media saturation was measured and related to the concentration. OxyMod sensors were placed at the exits of chambers 3 and 6 rather than after each chamber. This was done because the oxygen sensors occasionally trapped air bubbles that had the capacity to add oxygen to the media downstream. However, by spacing the sensors out more, the bubbles can exit the system, and their effect on the measured oxygen concentration changes can be minimized. Each sensor had a measured calibration curve that was applied to record oxygen saturation levels. The real-time data was recorded every 10 seconds for 60 seconds to measure the relative oxygen saturation percent values, resulting in 6 saturation readings. These readings were averaged to reduce noise in the readings and converted to concentrations using the calculated linear equation for further calculations. The oxygen uptake rate (OUR) was calculated as described by Felder et al. in Equation 3.1 [25].

The OUR per scaffold is defined as

$$OUR_{scaffold} = \left(C_{O_2,in} - C_{O_2,out}\right) * v \quad \textbf{Equation 3.1}$$

where $C_{o2,in}$ is the concentration of oxygen entering the chamber, $C_{o2,out}$ is the concentration of oxygen leaving the chamber, which are both in μmol/L, and v is the volumetric flow rate in L/hr. The OUR per cell was determined by Equation 3.2.

$$OUR_{cell} = \frac{OUR_{scaffold}}{N_{cell}} \quad \textbf{Equation 3.2}$$

In Equation 3.2, N_{cell} is the total number of cells in the scaffold.

3.2.4 Oxygen Sensor Calibration

Before each bioreactor run, the oxygen sensors were calibrated to 100% saturation and 0% saturation conditions. In the case of 100% saturation, the bioreactor was assembled with oxygen-permeable tubing, filled with DI water, and placed in the incubator for 12 hours. After 12 hours, the tau values for each sensor were recorded in the same way described in section 3.2.3 for measuring saturation levels. Alternatively, in the 0% saturation condition, the bioreactor was assembled using only one media vessel and oxygen-impermeable tubing. It was filled with DI water, and then a diffusing stone was connected to a nitrogen air tank and placed into the media vessel. This forced dissolved oxygen out of the system, creating a 0% saturation condition. After 4 hours, each sensor's tau values, or the fluorescent time constant measured from the RedEye patch, were recorded as described in section 3.2.3 for measuring saturation levels. The measured tau values were then applied to the two-point calibration curve in the NeoFox Viewer software for each sensor before oxygen saturation measurements.

3.2.5 Hydrogel Dimension Measurement

To measure the dimensions of each hydrogel scaffold, an image was taken with each hydrogel and a ruler for a known scale. This image was input into ImageJ, and each hydrogel's length, width, and height were calculated. Additionally, the percent change in volume was calculated based on the original 0.5 mL hydrogel solution volume. The volume of each scaffold was calculated using the formula for the volume of an elliptical cylinder (Equation 3.3). Photos of the hydrogel scaffold after the 4-day bioreactor run can be seen in Figure A2.1 and Figure A2.2 in the Appendix.

$$V = \pi ab\mathrm{h} \quad \boldsymbol{Equation\ 3.3}$$

Where:

$$V = Volume$$
$$a, b = radii$$
$$h = height$$

3.2.6 Cellularity Quantification

The cellularity quantification procedure was followed as previously described in section 2.2.5 with slight modification. In this case, live/dead viability was also quantified during counting with the hemocytometer. The total number of cells used in the oxygen uptake rate calculations included only live cells. This was done to accurately represent the per-cell oxygen uptake rate because the dead cells were not taking up oxygen.

3.2.7 Hydrogel Hypoxia Model

To better understand the hypoxia experienced individually within each hydrogel scaffold, a modified mathematical spheroid model was applied to calculate the size of the hypoxic core in each scaffold. The model was borrowed from Grimes et al. and was modified with empirically measured values for the diffusion of O_2 through collagen hydrogels from Colom et al. and the calculated oxygen uptake rates [26, 27]. The model considers a spheroid, such that cells comprise an entire sphere. The model, as described by Grimes et al., was derived initially from the diffusion equation and a consumption factor, written below as Equation 3.4.

$$\frac{\partial C}{\partial t} = D\nabla^2 C - a(r) \quad \textbf{Equation 3.4}$$

In the equation, *D* is the diffusion constant of the tissue, which in this case was 2.0 x 10^{-9} m^2/s, *C* is the volume of oxygen per unit mass, and *a(r)* is the oxygen consumption rate at point r [27]. For this model, the oxygen supply was assumed to be at a steady state, and *a(r)* was assumed constant throughout the spheroid, which did not affect estimations [26]. Rewriting this equation in terms of the spherical Laplacian yields Equation 3.5.

$$a(r) = \frac{D}{r^2}\frac{\partial}{\partial r}\left(r^2\frac{\partial C}{\partial r}\right) \quad \textbf{Equation 3.5}$$

This equation is solved by assuming the following boundary conditions:

$$C_o = Bulk\ media\ oxygen\ concentration$$

$$at\ r_n, C = 0\ and\ \frac{\partial C}{\partial r} = 0$$

and the solved equation is written as

$$C(r) = C_o + \frac{a}{6D}\left(r^2 - r_o^2 + 2r_n^3\left(\frac{1}{r} - \frac{1}{r_o}\right)\right) \quad \textbf{Equation 3.6}$$

where C is the volume of oxygen gas per unit of tumor mass. Finally, solving for r_n, or the anoxic limit within the spheroid (Figure 3.2), yields a fully analytical solution. Thus, setting $C(r_n) = 0$ allows for the equation to be written as

$$2r_c^3 - 3r_o r_c^2 + \frac{6DC_o r_o}{a} = 0 \quad \textbf{Equation 3.7}$$

The radius of an entirely viable spheroid is defined as r_l, whose equation is written below.

$$r_l = \sqrt{\frac{6Dp_o}{a\rho_T \rho_{O_2} K}} \quad \textbf{Equation 3.8}$$

In this equation, p_o is the dissolved oxygen partial pressure at the surface of the spheroid, assumed to be the same as the bulk dissolved oxygen partial pressure, ρ_T is the density of the spheroid, assumed to be the same as water, and ρ_{O2} is the density of oxygen gas at 1.331 kg m^{-3}. K is the Henry's Law constant previously calculated for oxygen concentration measurements of 1.04 mmol/L/atm. Equation 3.7 can be solved using trigonometric identities yielding the equation χ in terms of r_o.

$$\chi = \frac{arccos(1 - 2r_l^2/r_o^2) - 2\pi}{3} \quad \textbf{Equation 3.9}$$

Therefore, the radial thickness of the anoxic and normoxic/hypoxic regions are given as

$$r_c = r_o\left(\frac{1}{2} + \cos(\chi)\right) \quad \textbf{Equation 3.10}$$

and

$$r_n = r_o\left(\frac{1}{2} - \cos(\chi)\right). \quad \textbf{\textit{Equation 3.11}}$$

While the model is not a perfect fit for the geometry of the 3D hydrogel scaffolds used here, it can provide an estimate of the size of the anoxic region in each scaffold. Because oxygen concentrations were only measured after chambers 3 and 6, measurements were averaged for chambers 1-3 and 4-6 and assumed to be constant. For example, the oxygen consumption per cell was assumed to be the same for chambers 1-3 and 4-6, respectively. The bulk media oxygen concentration was calculated by assuming equal consumption per chamber and dividing total consumption by 3, and subtracting this consumption from the previous sensor's bulk oxygen concentration, measured or calculated, for the groups of chambers 1-3 and 4-6, respectively. Measured oxygen values were from day 4 because cellularity and viability were quantified simultaneously, giving the most accurate representation of these values. The average height of the hydrogel scaffolds (Table 3.1) was the model spheroid's diameter since this dimension was the smallest in all cases and would be the least restrictive regarding diffusional limitations.

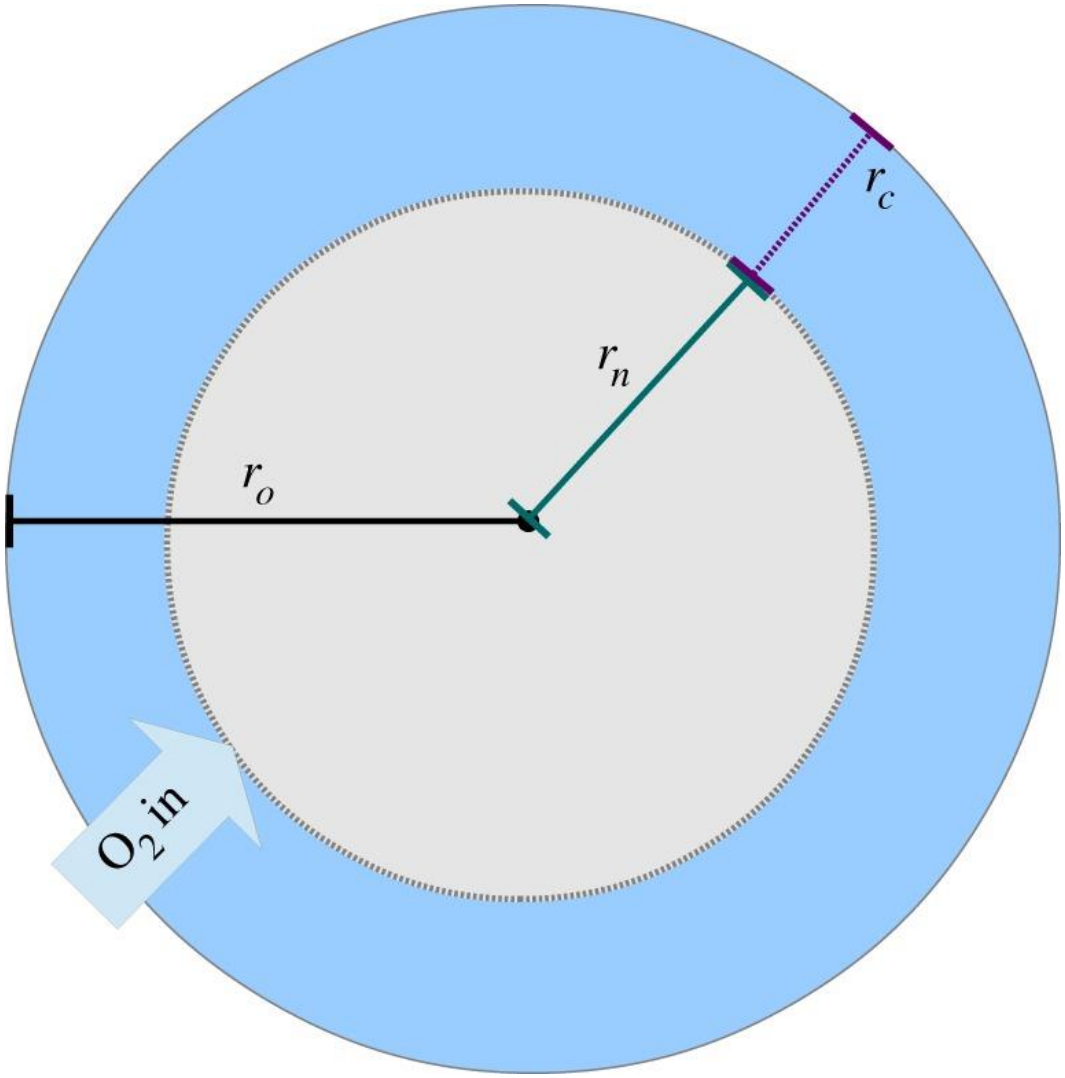

Figure 3.2: Hypoxia Spheroid Diagram

The diagram illustrates the different radii of the spheroid and what they represent. In this case, r_0 represents the total radius of the spheroid, r_n is the radius of the anoxic core, and r_c is the shell thickness of the hypoxic/normoxic region. The figure was used with permission from the following publication [26].

The calculated r_n from the model was used to determine the total volume of the anoxic region, and this value was used to determine the total percentage of the scaffold that was anoxic. If the cells in the scaffold were assumed to be homogenously distributed, this would give the

percentage of cells expected to be in anoxia and, therefore, dead. The volumes were calculated as spherical.

3.3 Results

3.3.1 Measured Oxygen Saturations

Figure 3.3 presents the measured oxygen saturation levels after chambers 3 and 6 throughout the 4 days. The oxygen saturation entering chamber 1 was assumed to be 100% based on previous measurements [25]. The oxygen saturation drop through chambers 1-3 is ~30% for all four days, and the drop through chambers 4-6 varies more but is ~20%. The oxygen consumption, therefore, did not change significantly during the 4 days. When looking at the oxygen consumption rate per cell (Figure 3.4), chambers 1-3 do not change significantly throughout the run, but chambers 4-6 appear to increase their oxygen consumption levels per cell.

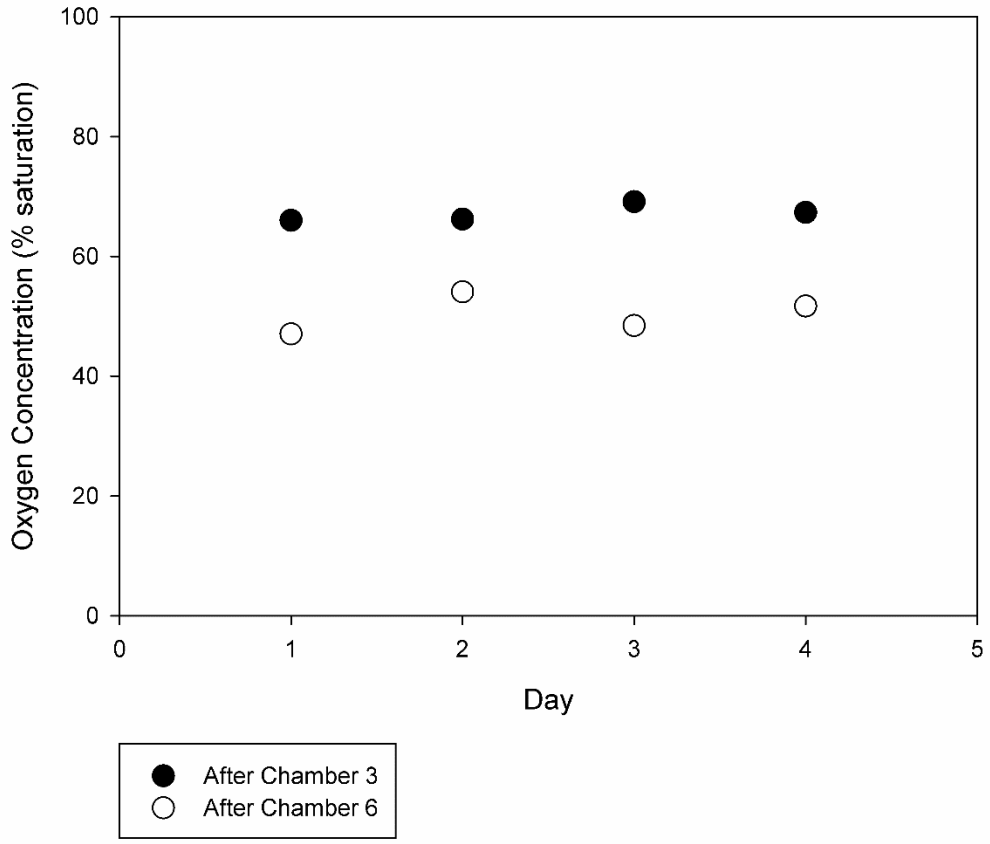

Figure 3.3: Oxygen Saturation throughout Daisy Chain Bioreactor Run

Percent oxygen saturation was measured in bulk media after chambers 3 and 6 for 4 days and plotted per day. This was done on a Daisy Chain (series) setup or runs where bulk media dissolved oxygen concentration surrounding hydrogel scaffolds varies as the media flows downstream in the series of chambers.

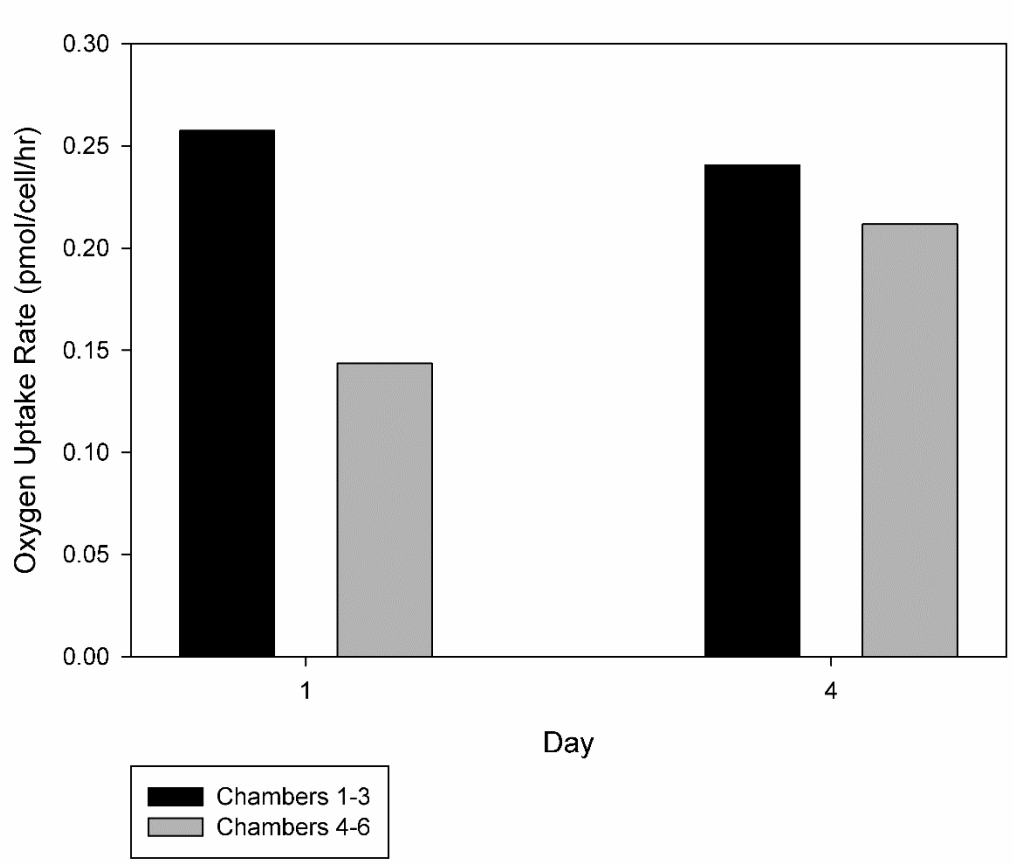

Figure 3.4: Cellular Oxygen Uptake Rate on Day 1 and Day 4

Each bar represents the average cellular oxygen uptake rate for cells before Chamber 3 (black), and for cells in chambers 4-6 (grey), values are reported in pmol/cell/hr. Oxygen uptake rates were calculated as specified by Felder et al. [25].

3.3.2 Cell Growth

The final cell amounts, percent growth, and viability were quantified for each hydrogel to determine the effects of variable oxygen concentrations on the proliferation rates of the cells. Figure 3.5 presents each final cell quantity versus the chamber number, which increases as oxygen saturation decreases. A clear downward trend can be seen in total cell numbers as the oxygen saturation level decreases. The dashed line represents the seeding cell quantity of each chamber. Figure 3.6 illustrates the percent growth of each scaffold plotted versus chamber

number, which also shows a downward trend, matching the final cell quantities. The percent viability of each scaffold was measured to validate the percent growth and final cell quantities. Again, a similar trend is seen where the percent viability decreases as the chamber number moves downstream (Figure 3.7).

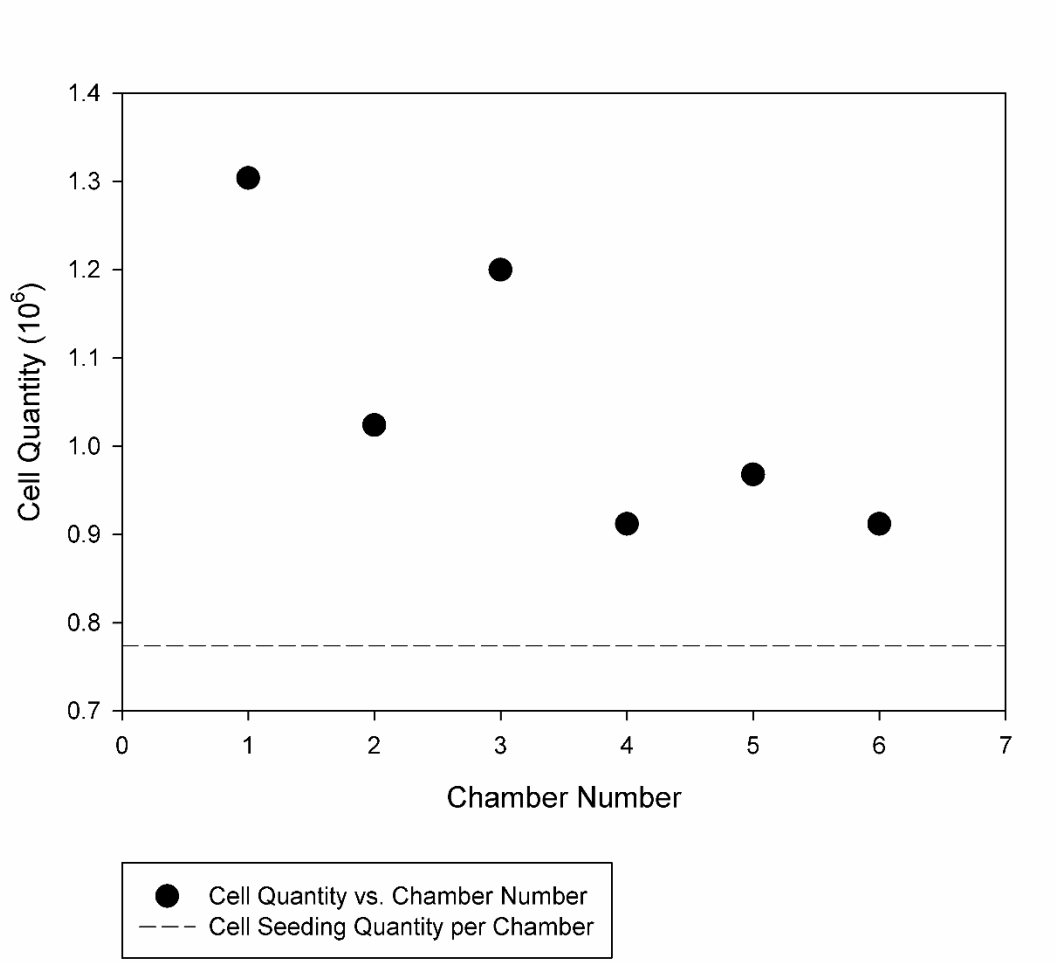

Figure 3.5: Final Cell Quantity vs. Chamber Number

The final cell quantity after the 4-day run is plotted against its chamber number. The chamber numbers increase as oxygen saturation decreases and as media moves downstream in the bioreactor. The light grey dashed line indicates the seeding cell quantity with which each chamber began the run.

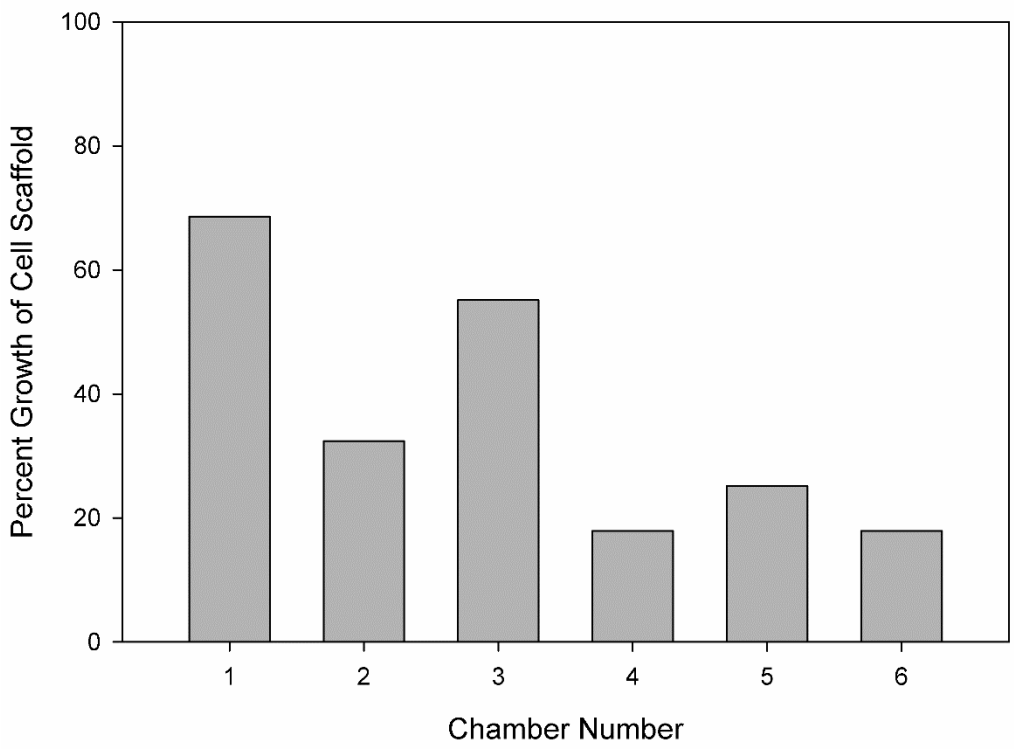

Figure 3.6: Percent Growth of Cell Scaffold in each Chamber

Cell quantity was quantified per chamber of a Daisy Chain (series) bioreactor run or runs where bulk media dissolved oxygen concentration surrounding hydrogel scaffolds varies as the media flows downstream in the series of chambers. A trend of lower cell growth with decreasing oxygen concentration was seen.

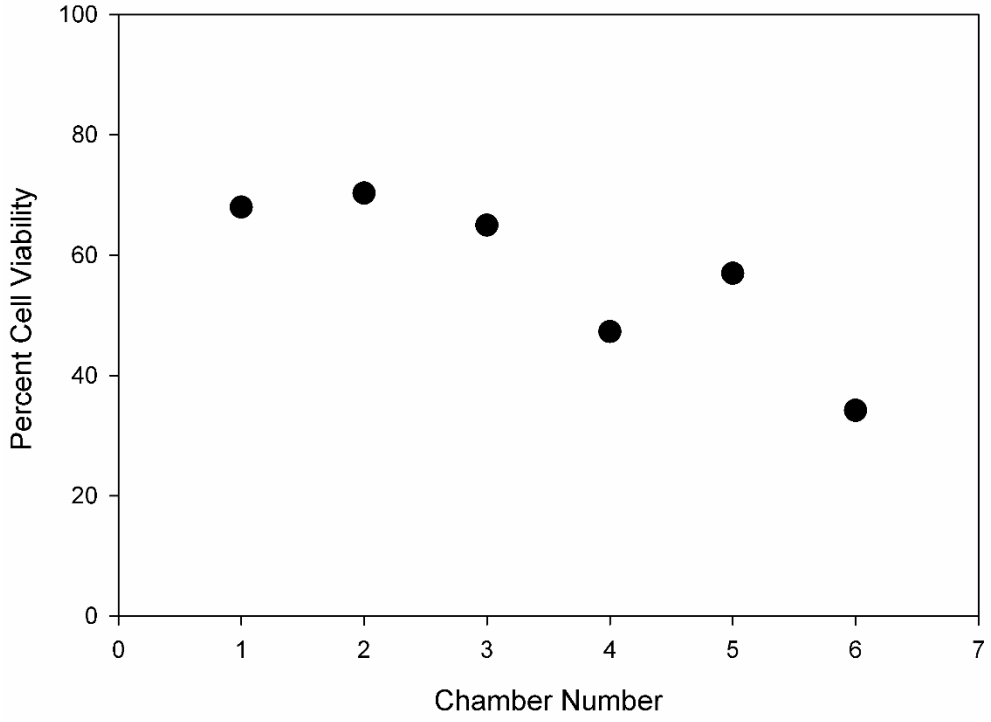

Figure 3.7: Percent Cell Viability vs. Chamber Number

Cell viability was calculated as $\left(\frac{\boldsymbol{live\ cells}}{\boldsymbol{live\ cells + dead\ cells}}\right)\boldsymbol{x100}$*. This was plotted against chamber number, which increases as oxygen saturation decreases and as media moves downstream in the bioreactor.*

3.3.3 Hydrogel Dimensions and Hypoxia Model

Notably, each hydrogel's volume changed significantly compared to the original volume. This change is likely due to flow and cellular remodeling/contraction and was quantified using a scale bar and the ImageJ software. The measured values are reported in Table 3.1, along with the percent change in volume based on the original 0.5 mL seeding volume. The highest percent change in volume was 83%, and the average percent change in volume was 71%. Generally, after the 4-day run, the hydrogel's geometrical shape most resembled an elliptical cylinder, which is

logical considering the bioreactor chambers are cylindrical. The elliptical nature is most likely due to the flow of media deforming the hydrogels into irregular shapes.

Table 3.1: Hydrogel Dimensions, Volume, and Percent Change in Volume on Day 4
Hydrogel Dimensions were measured by taking an image of each hydrogel with a ruler. The image was then imported into ImageJ, and dimensions were quantified. Volume was calculated using the formula for an elliptical cylinder. The percent change in volume is based on the original 0.5 mL volume of hydrogel solution.

Chamber	Radius a (mm)	Radius b (mm)	Height (mm)	Final Volume (mm^3)	Percent Change of Volume
1	5.263	3.904	2.936	189.5	62%
2	5.354	3.806	2.17	138.9	72%
3	5.827	3.433	1.85	116.3	77%
4	4.814	4.746	2.082	149.4	70%
5	7.355	3.697	2.113	180.5	64%
6	4.451	4.265	1.46	87.07	83%
Average	**5.511**	**3.975**	**2.102**	**143.6**	**71%**

The hypoxic core was estimated using the modified spheroid model, and Figure 3.8 plots the calculated depth into the hydrogel to reach the hypoxic core, r_c, according to Figure 3.2. The estimated radius of normoxic conditions decreases as chamber number increases and oxygen saturation levels decrease. These results mirror the measured cell growth trends and help explain why the percent viability trends downward with increasing chamber numbers. Table 3.2 lists the predicted percentage of the anoxic spheroid volume based on the calculated r_n values for each chamber.

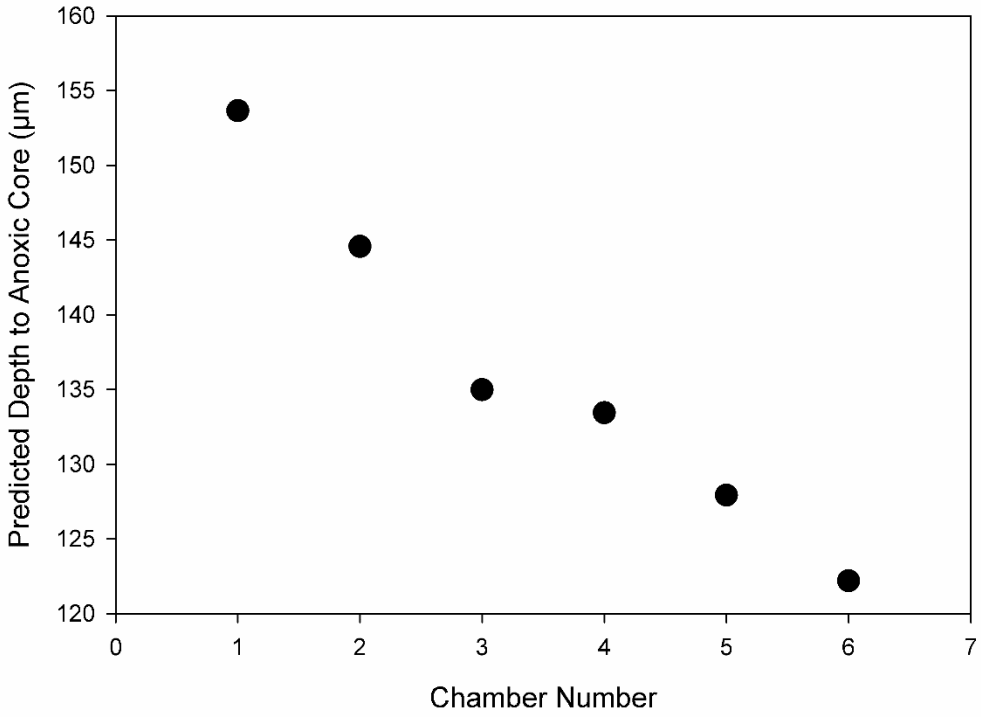

Figure 3.8: Depth into Hydrogel to Anoxic Core

Using the hypoxia model, the depth to reach the hypoxic core of each scaffold was calculated and plotted per chamber. The chamber number increases as oxygen saturation decreases and as media moves downstream in the bioreactor.

Table 3.2: Model Predicted Percentage of Anoxic Volume and Percent Viability per Chamber
The percentage of the total volume calculated to be anoxic was done based on the model's predicted r_n value and the spherical volume formula. The total volume was calculated using the average of hydrogel heights (Table 3.1) as the diameter of a sphere, which was 4.849 mm^3.

Chamber	Anoxic Region Volume (mm^3)	Percent Volume Anoxic	Estimated Percent Viability	Measured Percent Viability
1	3.017	62.2%	37.8%	68.0%
2	3.109	64.1%	35.9%	70.3%
3	3.209	66.2%	33.8%	65.0%
4	3.225	66.5%	33.5%	47.3%
5	3.284	67.7%	32.3%	57.0%
6	3.345	69.0%	31.0%	34.2%

3.4 Discussion

Each day during the 4-day bioreactor run, the bulk media oxygen saturation levels after chambers 3 and 6 were measured and plotted versus time in Figure 3.3, which shows a relatively consistent oxygen level drop during the experiment. One thing to note, the drop in oxygen saturation level is much lower for chambers 4-6 compared to chambers 1-3. The difference in oxygen level drop is most likely due to the increased size in the hypoxic region of each scaffold, which means that diffusion of oxygen into the scaffolds became increasingly more limited. Thus, the innermost cells couldn't consume oxygen, translating to a lower oxygen delta for chambers 4-6 because a smaller proportion of the total cells in the scaffold could consume oxygen. This sentiment is further explained by Figure 3.4, which plots the average per-cell oxygen uptake rates for chambers 1-3 and 4-6, respectively. When looking at Day 1 for both groups, chambers 1-3 show a higher per-cell oxygen uptake rate. On Day 4, the oxygen uptake rate is still higher

for chambers 1-3, but the gap is narrowed. A key difference between the two calculations is that on Day 4, the percentage of live versus dead cells was quantified and considered for both groups. As such, it can be assumed that the hypoxic/necrotic core of the scaffold was not as considered in this calculation, and mostly the outermost normoxic region was represented. In this region, the per-cell oxygen uptake rate was similar in both groups, indicating that the oxygenated cells did not alter their metabolism much due to the lower bulk oxygen saturation. Due to the unknown levels of cell death for each scaffold on days 1-3, the per-cell oxygen uptake rate is most likely an underestimate.

The effects on the cell proliferation of the decreased oxygen saturation levels in downstream media were also assessed. Figure 3.5 plots the final cell quantity for each scaffold against its corresponding chamber number, which increases as media moves further downstream in the bioreactor. This plot shows a negative trend in cell growth with decreased oxygen levels, which agrees with the idea of a larger hypoxic/necrotic core in these scaffolds. Furthermore, the growth percentage was also calculated and plotted per chamber in Figure 3.6, which again shows a trend of decreased cell proliferation in chambers downstream. The lowest reported growth percentage was seen in chamber 6, as expected, the chamber with the lowest level of bulk media oxygen, with a value of 18%. Interestingly, this value was also seen in chamber 4, a face that can be attributed to a difference in scaffold shapes, thus, oxygen concentration gradients. The percent viability, or the ratio of live cells to dead cells, was calculated for each chamber as an indication of a hypoxic core and to compare this characteristic between scaffolds. Figure 3.7 shows these values plotted against the chamber number. The percent viability of each scaffold decreases as the oxygen saturation level decreases and ranges from 70.3% to 34% in chambers 2 and 6, respectively. The change in percent viability between consecutive chambers does not appear

large enough to outweigh the expected noise due to the hydrogel shape and volume characteristics provided in Table 3.1. However, the change from chamber 1 to chamber 6 is large, indicating an apparent change in the hypoxic region of the scaffold.

Understanding the shape effects and size of the anoxic core of each scaffold is also required to ensure the repeatability and accuracy of the *in vitro* model. The dimensions with averages of each scaffold are listed in Table 3.1. The scaffolds most closely geometrically resembled an elliptical cylinder. Thus, the volume was calculated as an elliptical cylinder. The volumes of the hydrogels changed drastically throughout the run, showing, on average, 71% but up to 83% shrinkage. Scaffold shrinkage is expected in the case of hydrogels due to cell-ECM forces [28]. In this case, while not confirmed, fluid flow could have played a role in the hydrogel deformation [29]. Additionally, scaffold size and shape variations can also occur during the gelation and swelling, even with a mold [30]. Another important factor in nutrient diffusion is the total volume of the scaffold, which was found to have a large standard deviation with an average of 143.618 ± 38.649 mm^3. This variance between scaffolds can potentially explain measured cell growth and viability variations. For example, in Figure 3.6, chamber 3 shows higher percent growth than chamber 2, which goes against the overall negative trend. However, when cross-referenced with Table 3.1, the scaffold in chamber 3 has a smaller volume than the previous two chambers, possibly accounting for some of the measured noise. Estimating the size of this anoxic region is also crucial for estimating the number of cells in this region. As a method of predicting the size of the hypoxic core, a spheroid model was adapted by applying empirically measured data for the oxygen uptake rates of the EMT6 cell line and diffusion of oxygen in high-concentration (4 mg/mL) collagen hydrogels. While the scaffolds do not necessarily match the intended geometry of the model, the modified model does show how quickly the oxygen

saturation level drops to anoxic levels. The precited depth into the scaffold required to reach the hypoxic region is plotted in Figure 3.8, which mirrors the measured oxygen and cell data. The model predicts higher anoxia in downstream scaffolds, confirmed by cell viability and percent growth. When comparing Table 3.2 with the measured percent cell viability the model predicts a higher level of anoxia, thus cell death, than empirically measured in all scaffolds except chamber 6. Again, this most likely comes down to the shape and size effects that the model cannot consider.

3.5 Conclusion

One of the major goals of this study was to incorporate varied oxygen saturation conditions in the modified bioreactor. Additionally, we aimed to determine the effects of the varied oxygen saturation levels on the EMT6 cell line to create a better *in vitro* solid tumor model. Bulk media oxygen saturation levels were measured utilizing previously optimized optical oxygen sensors and a modified version of the previously used flow-perfusion bioreactor [25]. The bioreactor was modified to accommodate 3D collagen hydrogel scaffolds as a potential 3D solid tumor model. While more representative of the pathophysiology involved in solid tumors, hypoxia, a significant component of this pathophysiology, has not been incorporated in previous studies. Due to the significance of hypoxic effects in solid tumors, valid *in vitro* tumor models should incorporate this characteristic. Varying oxygen saturation levels were created inside the bioreactor by connecting the tubing so that the media flowed through each scaffold without reoxygenation in series, such that the oxygen saturation was lowered step-wise. Optical oxygen sensors strategically placed after chambers 3 and 6 confirmed the drop in oxygen saturation levels. Furthermore, the result of increasingly lower oxygen saturation levels was determined by analyzing each scaffold's cell number, percent growth, and viability. The results

showed lower growth percentages and lower viability in downstream scaffolds, confirming the predicted increased size in hypoxic regions in these scaffolds. Lastly, we applied a modified spheroid model to the empirically measured data to better understand how large the anoxic region in each scaffold would be. The model predicted larger anoxic regions in scaffolds downstream, but the effects of different scaffold shapes/volumes on oxygen diffusion could not be included, possibly accounting for some measured noise in cell growth and viability. While predicted anoxic regions were larger than the measured percent cell viability, the model still helps provide a useful understanding of how quickly oxygen concentrations can drop within the hydrogel scaffolds.

In the future, this model can be combined with measured data to estimate the percent cell viability and amount of anoxia in each scaffold in real time. Additionally, histology and hypoxia staining should be performed to confirm the validity of the modified spheroid model. The scaffold mesh holder should be redesigned as a spherical shape to keep scaffold deformation in the shape of a spheroid. Along these lines, a sphere mold should be used when forming the scaffold. These changes would allow the scaffolds to fit the model better than the current geometry, assuming the observed deformation during the culture period would not result in departures from the model's implied sphericity. Lastly, exploring different cell seeding quantities would be beneficial to determine what would most accurately represent a solid tumor.

3.6 References

[1] M. R. Horsman and P. Vaupel, "Pathophysiological Basis for the Formation of the Tumor Microenvironment," *Frontiers in Oncology,* vol. 6, Apr 2016, Art no. 66, doi: 10.3389/fonc.2016.00066.

[2] B. Arneth, "Tumor Microenvironment," *Medicina,* vol. 56, no. 1, p. 15, 2019, doi: 10.3390/medicina56010015.

[3] G. Hassan and M. Seno, "Blood and Cancer: Cancer Stem Cells as Origin of Hematopoietic Cells in Solid Tumor Microenvironments," *Cells,* vol. 9, no. 5, p. 1293, 2020, doi: 10.3390/cells9051293.

[4] C.-H. Heldin, K. Rubin, K. Pietras, and A. Östman, "High interstitial fluid pressure — an obstacle in cancer therapy," *Nature Reviews Cancer,* vol. 4, no. 10, pp. 806-813, 2004, doi: 10.1038/nrc1456.

[5] R. Gutmann *et al.*, "Interstitial hypertension in head and neck tumors in patients: correlation with tumor size," (in eng), *Cancer Res,* vol. 52, no. 7, pp. 1993-5, Apr 1 1992.

[6] M. Milosevic *et al.*, "Interstitial fluid pressure predicts survival in patients with cervix cancer independent of clinical prognostic factors and tumor oxygen measurements," (in eng), *Cancer Res,* vol. 61, no. 17, pp. 6400-5, Sep 1 2001.

[7] A. I. Minchinton and I. F. Tannock, "Drug penetration in solid tumours," (in en), *Nat Rev Cancer,* vol. 6, no. 8, pp. 583-92, Aug 2006, doi: 10.1038/nrc1893.

[8] C. A. Klebanoff, L. Gattinoni, and N. P. Restifo, "CD8+ T-cell memory in tumor immunology and immunotherapy," *Immunological Reviews,* vol. 211, no. 1, pp. 214-224, 2006, doi: 10.1111/j.0105-2896.2006.00391.x.

[9] H. Dong *et al.*, "Tumor-associated B7-H1 promotes T-cell apoptosis: A potential mechanism of immune evasion," *Nature Medicine,* vol. 8, no. 8, pp. 793-800, 2002, doi: 10.1038/nm730.

[10] T. Wang *et al.*, "Regulation of the innate and adaptive immune responses by Stat-3 signaling in tumor cells," *Nature Medicine,* vol. 10, no. 1, pp. 48-54, 2004, doi: 10.1038/nm976.

[11] D. Hanahan and Robert, "Hallmarks of Cancer: The Next Generation," *Cell,* vol. 144, no. 5, pp. 646-674, 2011, doi: 10.1016/j.cell.2011.02.013.

[12] B.-Z. Qian and J. W. Pollard, "Macrophage Diversity Enhances Tumor Progression and Metastasis," *Cell,* vol. 141, no. 1, pp. 39-51, 2010, doi: 10.1016/j.cell.2010.03.014.

[13] A. Mantovani, P. Allavena, A. Sica, and F. Balkwill, "Cancer-related inflammation," *Nature,* vol. 454, no. 7203, pp. 436-444, 2008, doi: 10.1038/nature07205.

[14] Y. Ohue and H. Nishikawa, "Regulatory T (Treg) cells in cancer: Can Treg cells be a new therapeutic target?," *Cancer Science,* vol. 110, no. 7, pp. 2080-2089, 2019, doi: 10.1111/cas.14069.

[15] Y. Chen, K. M. McAndrews, and R. Kalluri, "Clinical and therapeutic relevance of cancer-associated fibroblasts," *Nature Reviews Clinical Oncology,* vol. 18, no. 12, pp. 792-804, 2021, doi: 10.1038/s41571-021-00546-5.

[16] M. Desbois and Y. Wang, "Cancer-associated fibroblasts: Key players in shaping the tumor immune microenvironment," *Immunological Reviews,* vol. 302, no. 1, pp. 241-258, 2021, doi: 10.1111/imr.12982.

[17] X. Jing *et al.*, "Role of hypoxia in cancer therapy by regulating the tumor microenvironment," *Molecular Cancer,* vol. 18, no. 1, 2019, doi: 10.1186/s12943-019-1089-9.

[18] E. E. Wicks and G. L. Semenza, "Hypoxia-inducible factors: cancer progression and clinical translation," *Journal of Clinical Investigation,* vol. 132, no. 11, 2022, doi: 10.1172/jci159839.

[19] M. H.-R. Bao and C. C.-L. Wong, "Hypoxia, Metabolic Reprogramming, and Drug Resistance in Liver Cancer," *Cells,* vol. 10, no. 7, p. 1715, 2021, doi: 10.3390/cells10071715.

[20] M. Z. Noman *et al.*, "PD-L1 is a novel direct target of HIF-1α, and its blockade under hypoxia enhanced MDSC-mediated T cell activation," *Journal of Experimental Medicine,* vol. 211, no. 5, pp. 781-790, 2014, doi: 10.1084/jem.20131916.

[21] G. Multhoff and P. Vaupel, "Hypoxia Compromises Anti-Cancer Immune Responses," Springer International Publishing, 2020, pp. 131-143.

[22] A. D. Simmons and V. I. Sikavitsas, "Monitoring Bone Tissue Engineered (BTE) Constructs Based on the Shifting Metabolism of Differentiating Stem Cells," (in eng), *Ann Biomed Eng,* vol. 46, no. 1, pp. 37-47, Jan 2018, doi: 10.1007/s10439-017-1937-y.

[23] O. Optics, "NeoFox Phase Fluorometer Installation and Operation Manual," ed, 2010.

[24] R. Sander, "Compilation of Henry's law constants (version 4.0) for water as solvent," *Atmos. Chem. Phys.,* vol. 15, no. 8, pp. 4399-4981, 2015, doi: 10.5194/acp-15-4399-2015.

[25] M. L. Felder, A. D. Simmons, R. L. Shambaugh, and V. I. Sikavitsas, "Effects of Flow Rate on Mesenchymal Stem Cell Oxygen Consumption Rates in 3D Bone-Tissue-Engineered Constructs Cultured in Perfusion Bioreactor Systems," (in en), *Fluids,* vol. 5, no. 1, p. 30, 2020/3 2020, doi: 10.3390/fluids5010030.

[26] D. R. Grimes, C. Kelly, K. Bloch, and M. Partridge, "A method for estimating the oxygen consumption rate in multicellular tumour spheroids," *Journal of The Royal Society Interface,* vol. 11, no. 92, p. 20131124, 2014, doi: 10.1098/rsif.2013.1124.

[27] A. Colom, R. Galgoczy, I. Almendros, A. Xaubet, R. Farré, and J. Alcaraz, "Oxygen diffusion and consumption in extracellular matrix gels: Implications for designing three-dimensional cultures," *Journal of Biomedical Materials Research Part A,* vol. 102, no. 8, pp. 2776-2784, 2014, doi: 10.1002/jbm.a.34946.

[28] P. Hameed and G. Manivasagam, "An overview of bio-actuation in collagen hydrogels: a mechanobiological phenomenon," (in eng), *Biophys Rev,* vol. 13, no. 3, pp. 387-403, Jun 2021, doi: 10.1007/s12551-021-00804-x.

[29] F. P. Duda, A. C. Souza, and E. Fried, "Fluid flow and interface motion in gels: A finite-strain theory and its application to a channel flow problem," *Journal of the Mechanics and Physics of Solids,* vol. 155, p. 104566, 2021/10/01/ 2021, doi: https://doi.org/10.1016/j.jmps.2021.104566.

[30] E. Fennell and J. M. Huyghe, "Chemically Responsive Hydrogel Deformation Mechanics: A Review," *Molecules,* vol. 24, no. 19, p. 3521, 2019, doi: 10.3390/molecules24193521.

Appendix

A1. Supplemental Methodologies

A1.1 Acetaldehyde Concentration Measurement

Acetaldehyde concentrations in the headspace of culture media samples were measured by bubbling laboratory air at a rate of 100 ml/min through about 40 ml of culture media contained in a 50 ml Erlenmeyer flask and passing the output through the Herriott gas cell of the laser spectrometer. The Erlenmeyer flask was placed in a temperature-controlled water bath during measurements, and an empty Erlenmeyer flask was used to trap any liquid carried by the flowing air. A cold trap consisting of a coiled section of ¼" Teflon tubing about 1 meter in length immersed in ice water was placed between the liquid trap flask and the mass flow controller at the entry to the Herriott gas cell. Data collection involved saving a background spectrum before the initiation of headspace sampling and then saving a sample spectrum at 3 minutes and a second sample spectrum at 4 minutes following the initiation of headspace sampling. This time span was sufficient to fill the 3.2-liter volume Herriott gas cell at a 20 torr pressure with a representative headspace vapor sample. The liquid trapping flask and the Teflon tubing for the cold trap were rinsed with water and dried with compressed air between measurements of different cell culture media samples. Acetaldehyde concentrations were determined by subtracting the background spectrum from the headspace sample spectrum and multiplying the peak-to-peak voltages for the two most substantial acetaldehyde peaks by the calibration factors obtained with the 20 ppm acetaldehyde reference gas sample shown in Figure 2.2.

A2. Supplemental Material

A2.1 Collagen Hydrogel Images

Figure A2.1: Collagen Hydrogel Top View with Scale

An image taken from the top view of the collagen hydrogels after the 4-day bioreactor run. This view is where the two radii, a and b, were measured.

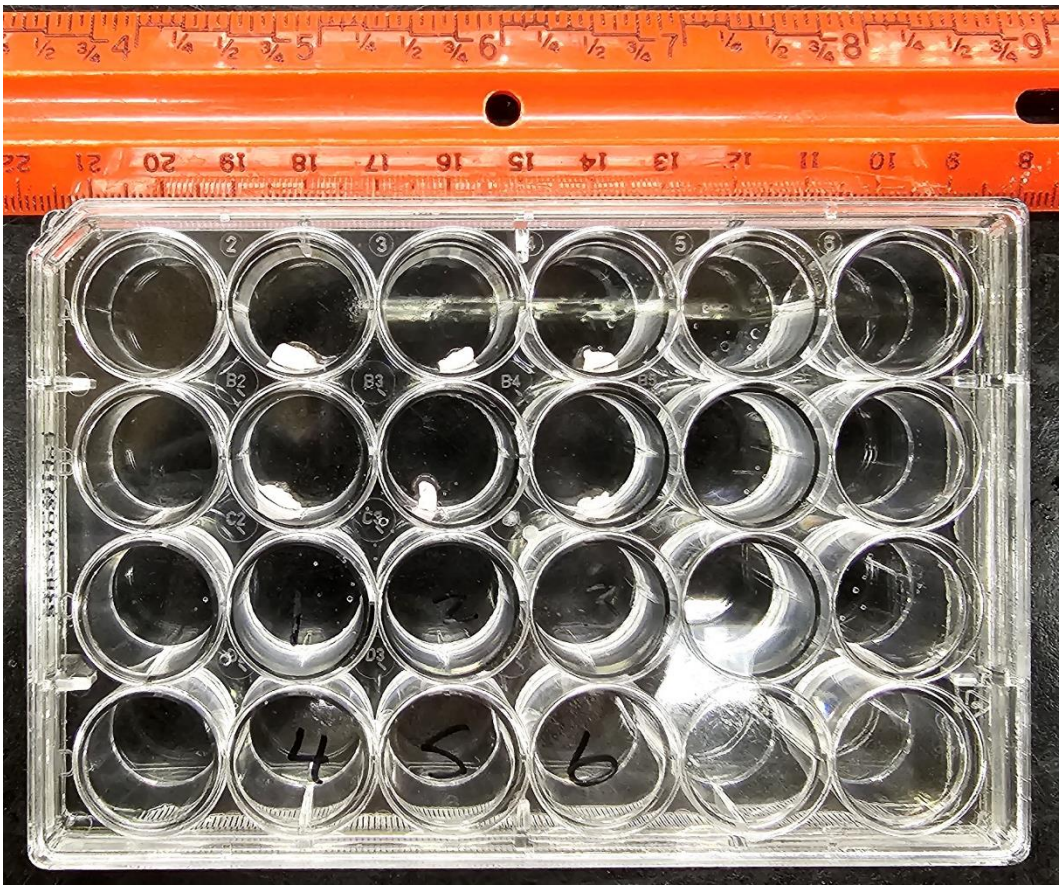

Figure A2.2: Collagen Hydrogel Side View with Scale

An image taken from the side view of the collagen hydrogels after the 4-day bioreactor run. This view is where the height of each scaffold was measured.

A2.2 Oxygen Saturation to Concentration Curve

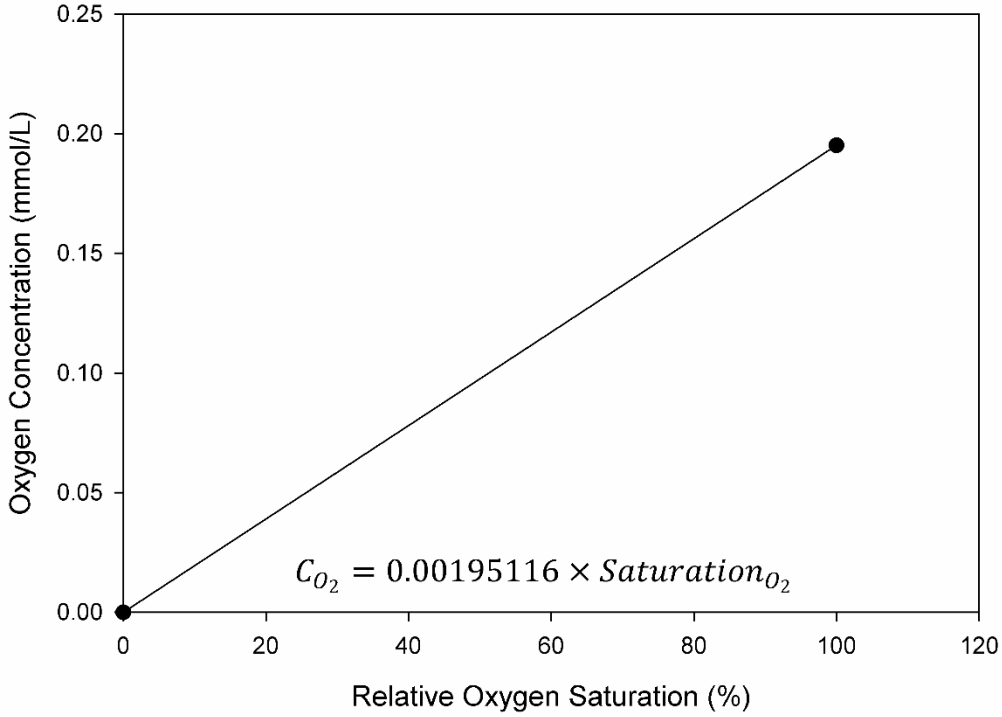

Figure A2.3: Oxygen Concentration vs. Relative Oxygen Saturation

The plotted linear curve used to calculate the concentration of dissolved O_2 from the measured relative oxygen saturation values of the OxyMod sensors.